
1 “Soft” Chemical Synthesis and Manipulation of Semiconductor Nanocrystals

Jennifer A. Hollingsworth and Victor I. Klimov

CONTENTS

1.1	Introduction	2
1.2	Colloidal Nanosynthesis	4
1.2.1	Tuning Particle Size and Maintaining Size Monodispersity	5
1.2.2	CdSe NQDs: The “Model” System.....	7
1.2.3	Optimizing Photoluminescence.....	8
1.2.4	Aqueous-Based Synthetic Routes and the Inverse-Micelle Approach.....	9
1.3	Inorganic Surface Modification	13
1.3.1	(Core)Shell NQDs	13
1.3.2	Giant-Shell NQDs.....	19
1.3.3	Quantum-Dot/Quantum-Well Structures	22
1.3.4	Type-II and Quasi-Type-II (Core)Shell NQDs.....	26
1.4	Shape Control	26
1.4.1	Kinetically Driven Growth of Anisotropic NQD Shapes: CdSe as the Model System	27
1.4.2	Shape Control Beyond CdSe	31
1.4.3	Focus on Heterostructured Rod and Tetrapod Morphologies.....	36
1.4.4	Solution–Liquid–Solid Nanowire Synthesis.....	37
1.5	Phase Transitions and Phase Control.....	37
1.5.1	NQDs under Pressure	37
1.5.2	NQD Growth Conditions Yield Access to Nonthermodynamic Phases	39
1.6	Nanocrystal Doping.....	41
1.7	Nanocrystal Assembly and Encapsulation	49

Acknowledgment	57
References	57

1.1 INTRODUCTION

An important parameter of a semiconductor material is the width of the energy gap that separates the conduction from the valence energy bands ([Figure 1.1a, left](#)). In semiconductors of macroscopic sizes, the width of this gap is a fixed parameter, which is determined by the material's identity. However, the situation changes in the case of nanoscale semiconductor particles with sizes less than ~10 nm ([Figure 1.1a, right](#)). This size range corresponds to the regime of quantum confinement for which electronic excitations “feel” the presence of the particle boundaries and respond to changes in the particle size by adjusting their energy spectra. This phenomenon is known as the *quantum size effect*, whereas nanoscale particles that exhibit it are often referred to as quantum dots (QDs).

As the QD size decreases, the energy gap increases, leading, in particular, to a blue shift of the emission wavelength. In the first approximation, this effect can be described using a simple “quantum box” model. For a spherical QD with radius R, this model predicts that the size-dependent contribution to the energy gap is simply proportional to $1/R^2$ ([Figure 1.1b](#)). In addition to increasing energy gap, quantum confinement leads to a collapse of the continuous energy bands of the bulk material into discrete, “atomic” energy levels. These well-separated QD states can be labeled using atomic-like notations (1S, 1P, 1D, etc.), as illustrated in [Figure 1.1a](#). The discrete structure of energy states leads to the discrete absorption spectrum of QDs ([schematically shown by vertical bars in Figure 1.1c](#)), which is in contrast to the continuous absorption spectrum of a bulk semiconductor ([Figure 1.1c](#)).

Semiconductor QDs bridge the gap between cluster molecules and bulk materials. The boundaries between molecular, QD, and bulk regimes are not well defined and are strongly material dependent. However, a range from ~100 to ~10,000 atoms per particle can be considered as a crude estimate of sizes for which the nanocrystal regime occurs. The lower limit of this range is determined by the stability of the bulk crystalline structure with respect to isomerization into molecular structures. The upper limit corresponds to sizes for which the energy level spacing is approaching the thermal energy kT , meaning that carriers become mobile inside the QD.

Semiconductor QDs have been prepared by a variety of “physical” and “chemical” methods. Some examples of physical processes, characterized by high energy input, include molecular-beam-epitaxy (MBE) and metalorganic-chemical-vapor-deposition (MOCVD) approaches to QDs,^{1,2,3} and vapor-liquid-solid (VLS) approaches to quantum wires.^{4,5} High-temperature methods have also been applied to chemical routes, including particle growth in glasses.^{6,7} Here, however, the emphasis is on “soft” (low-energy-input) colloidal chemical synthesis of crystalline semiconductor nanoparticles that will be referred to as nanocrystal quantum dots (NQDs). NQDs comprise an inorganic core overcoated with a layer of organic ligand molecules. The organic capping provides electronic and chemical passivation of surface dangling bonds, prevents uncontrolled growth and agglomeration of the nanoparticles, and allows NQDs to be chemically manipulated like large

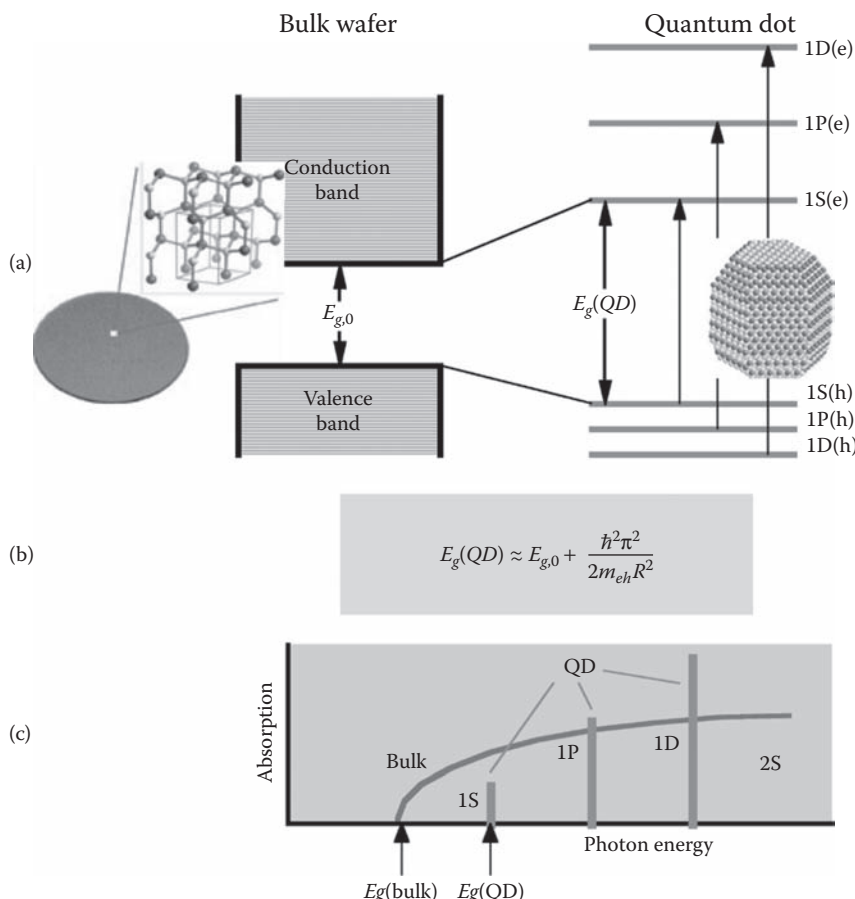


FIGURE 1.1 (a) A bulk semiconductor has continuous conduction and valence energy bands separated by a fixed energy gap, $E_{g,0}$ (left), while a QD is characterized by discrete atomic-like states with energies that are determined by the QD radius R (right). (b) The expression for the size-dependent separation between the lowest electron [1S(e)] and hole [1S(h)] QD states (QD energy gap) obtained using the “quantum box” model [$m_{eh} = m_e m_h / (m_e + m_h)$, where m_e and m_h are effective masses of electrons and holes, respectively]. (c) A schematic representation of the continuous absorption spectrum of a bulk semiconductor (curved line), compared to the discrete absorption spectrum of a QD (vertical bars).

molecules with solubility and reactivity determined by the identity of the surface ligand. In contrast to substrate-bound epitaxial QDs, NQDs are “freestanding.” This discussion concentrates on the most successful synthesis methods, where success is determined by high crystallinity, adequate surface passivation, solubility in nonpolar or polar solvents, and good size monodispersity. Size monodispersity permits the study and, ultimately, the use of materials-size-effects to define novel materials properties. Monodispersity in terms of colloidal nanoparticles (1–15 nm

size range) requires a sample standard deviation of $\sigma \leq 5\%$, which corresponds to \pm one lattice constant.⁸ Although colloidal monodispersity in this strict sense is increasingly common, preparations are also included in this chapter that achieve approximately $\sigma \leq 20\%$, in particular where other attributes, such as novel compositions or shape control, are relevant. In addition, “soft” approaches to NQD chemical and structural modification as well as to NQD assembly into artificial solids or artificial molecules are discussed.

1.2 COLLOIDAL NANOSYNTHESIS

The most successful NQD preparations in terms of quality and monodispersity entail pyrolysis of metal-organic precursors in hot coordinating solvents (120°C–360°C). Generally understood in terms of La Mer and Dinegar’s studies of colloidal particle nucleation and growth,^{8,9} these preparative routes involve a temporally discrete nucleation event followed by relatively rapid growth from solution-phase monomers and finally slower growth by Ostwald ripening (referred to as recrystallization or aging) (Figure 1.2). Nucleation is achieved by quick injection of precursor into the hot coordinating solvents, resulting in thermal decomposition of the precursor reagents and supersaturation of the formed “monomers” that is partially

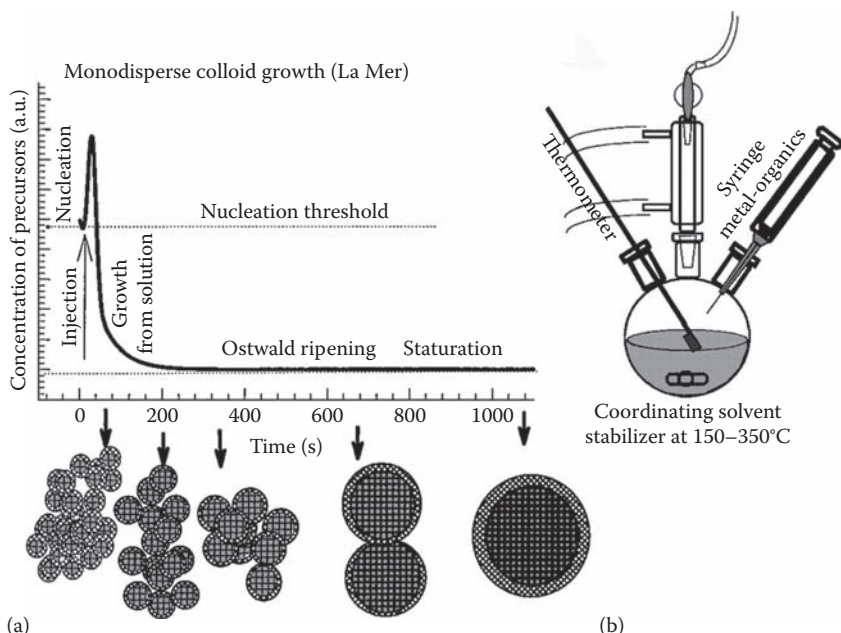


FIGURE 1.2 (a) Schematic illustrating La Mer’s model for the stages of nucleation and growth for monodisperse colloidal particles. (b) Representation of the synthetic apparatus employed in the preparation of monodisperse NQDs. (Reprinted with permission from Murray, C. B., C. R. Kagan, and M. G. Bawendi, *Annu. Rev. Mater. Sci.*, 30, 545, 2000.)

relieved by particle generation. Growth then proceeds by addition of monomer from solution to the NQD nuclei. Monomer concentrations are below the critical concentration for nucleation, and, thus, these species only add to existing particles, rather than form new nuclei.¹⁰ Once monomer concentrations are sufficiently depleted, growth can proceed by Ostwald ripening. Here, sacrificial dissolution of smaller (higher-surface-energy) particles results in growth of larger particles and, thereby, fewer particles in the system.⁸ Recently, a more precise understanding of the molecular-level mechanism of “precursor evolution” has been described for II-VI¹¹ and IV-VI¹² NQDs. Further, it has also been proposed that the traditional La Mer model is not valid for hot-injection synthesis schemes because nucleation, ripening, and growth may occur almost concurrently. Moreover, the presence of strongly coordinating ligands may also alter nucleation and growth processes, further complicating the simple interpretation of reaction events.¹³ Finally, a modification of the Ostwald ripening process has also been described wherein the particle *concentration* decreases substantially during the growth process. This process has been called “self-focusing.”^{14,15}

Alternatively, supersaturation and nucleation can be triggered by a *slow* ramping of the reaction temperature. Precursors are mixed at low temperature and slowly brought to the temperature at which precursor reaction and decomposition occur sufficiently quickly to result in supersaturation.¹⁶ Supersaturation is again relieved by a “nucleation burst,” after which temperature is controlled to avoid additional nucleation events, allowing monomer addition to existing nuclei to occur more rapidly than new monomer formation. Thus, nucleation does not need to be instantaneous, but in most cases it should be a single, temporally discreet event to provide for the desired nucleation-controlled narrow size dispersions.¹⁰

1.2.1 TUNING PARTICLE SIZE AND MAINTAINING SIZE MONODispersity

Size and size dispersion can be controlled during the reaction, as well as postpreparatively. In general, time is a key variable; longer reaction times yield larger average particle size. Nucleation and growth temperatures play contrasting roles. *Lower* nucleation temperatures support lower monomer concentrations and can yield larger-size nuclei. Whereas, *higher* growth temperatures can generate larger particles as the rate of monomer addition to existing particles is enhanced. Also, Ostwald ripening occurs more readily at higher temperatures. Precursor concentration can influence both the nucleation and the growth process, and its effect is dependent on the surfactant/precursor-concentration ratio and the identity of the surfactants (i.e., the strength of interaction between the surfactant and the NQD or between the surfactant and the monomer species). All else being equal, higher precursor concentrations promote the formation of fewer, larger nuclei and, thus, larger NQD particle size. Similarly, low stabilizer:precursor ratios yield larger particles. Also, weak stabilizer-NQD binding supports growth of large particles and, if too weakly coordinating, agglomeration of particles into insoluble aggregates.¹⁰ Stabilizer–monomer interactions may influence growth processes, as well. Ligands that bind strongly to monomer species may permit unusually high monomer concentrations that are required for very fast growth (see Section 1.3),¹⁷ or they may promote reductive elimination of the metal species (see later).¹⁸

The steric bulk of the coordinating ligands can impact the rate of growth subsequent to nucleation. Coordinating solvents typically comprise alkylphosphines, alkylphosphine oxides, alkylamines, alkylphosphates, alkylphosphites, alkylphosphonic acids, alkylphosphoramide, alkylthiols, fatty acids, etc., of various alkyl chain lengths and degrees of branching. The polar head group coordinates to the surface of the NQD, and the hydrophobic tail is exposed to the external solvent/matrix. This interaction permits solubility in common nonpolar solvents and hinders aggregation of individual nanocrystals by shielding the van der Waals attractive forces between NQD cores that would otherwise lead to aggregation and flocculation. The NQD-surfactant connection is dynamic, and monomers can add or subtract relatively unhindered to the crystallite surface. The ability of component atoms to reversibly come on and off of the NQD surface provides a necessary condition for high crystallinity—particles can anneal while particle aggregation is avoided. Relative growth rates can be influenced by the steric bulk of the coordinating ligand. For example, during growth, bulky surfactants can impose a comparatively high steric hindrance to approaching monomers, effectively reducing growth rates by decreasing diffusion rates to the particle surface.¹⁰

The two stages of growth (the relatively rapid first stage and Ostwald ripening) differ in their impact on size dispersity. During the first stage of growth, size distributions remain relatively narrow (dependent on the nucleation event) or can become more focused, whereas during Ostwald ripening, size tends to defocus as smaller particles begin to shrink and, eventually, dissolve in favor of growth of larger particles.¹⁹ The benchmark preparation for CdS, CdSe, and CdTe NQDs,²⁰ which dramatically improved the total quality of the nanoparticles prepared until that point, relied on Ostwald ripening to generate size series of II-VI NQDs. For example, CdSe NQDs from 1.2 to 11.5 nm in diameter were prepared.²⁰ Size dispersions of 10%–15% were achieved for the larger-size particles and had to be subsequently narrowed by size-selective precipitation. The size-selective process simply involves first titrating the NQDs with a polar “nonsolvent,” typically methanol, to the first sign of precipitation plus a small excess, resulting in precipitation of a small fraction of the NQDs. Such controlled precipitation preferentially removes the largest NQDs from the starting solution, as these become unstable to solvation before the smaller particles do. The precipitate is then collected by centrifugation, separated from the liquids, redissolved, and precipitated again. This iterative process separates larger from smaller NQDs and can generate the desired size dispersion of $\leq 5\%$.

Preparations for II-VI semiconductors have also been developed that specifically avoid the Ostwald-ripening growth regime. These methods maintain the regime of relatively fast growth (the “size-focusing” regime) by adding additional precursor monomer to the reaction solution after nucleation and before Ostwald growth begins. The additional monomer is not sufficient to nucleate more particles, that is, it is not sufficient to again surpass the nucleation threshold. Instead, monomers add to existing particles and promote relatively rapid particle growth. Sizes focus as monomer preferentially adds to smaller particles rather than to larger ones.¹⁹ The high monodispersity is evident in transmission electron micrograph (TEM) imaging ([Figure 1.3](#)). Alternatively, growth is stopped during the fast-growth stage (by removing the heat source), and sizes are limited to those relatively close to

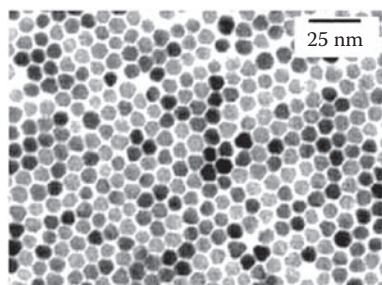


FIGURE 1.3 TEM of 8.5 nm diameter CdSe nanocrystals demonstrating the high degree of size monodispersity achieved by the “size-focusing” synthesis method. (Reprinted with permission from Peng, X., J. Wickham, and A.P. Alivisatos, *J. Am. Chem Soc.*, 120, 5343, 1998.)

the initial nucleation size. Because nucleation size can be manipulated by changing precursor concentration or reaction injection temperature, narrow size dispersions of controlled average particle size can be obtained by simply stopping the reaction shortly following nucleation, during the rapid-growth stage.

1.2.2 CdSe NQDs: THE “MODEL” SYSTEM

Owing to the ease with which high-quality samples can be prepared, the II-VI compound, CdSe, has comprised the “model” NQD system and been the subject of much basic research into the electronic and optical properties of NQDs. CdSe NQDs can be reliably prepared from pyrolysis of a variety of cadmium precursors, including alkyl cadmium compounds (e.g., dimethylcadmium)²⁰ and various cadmium salts (e.g., cadmium oxide, cadmium acetate, and cadmium carbonate),²¹ combined with a selenium precursor prepared simply from Se powder dissolved in trioctylphosphine (TOP) or tributylphosphine (TBP). Initially, the surfactant–solvent combination, technical-grade trioctylphosphine oxide (TOPO) and TOP, was used, where tech-TOPO performance was batch specific due to the relatively random presence of adventitious impurities.²⁰ More recently, tech-TOPO has been replaced with “pure” TOPO to which phosphonic acids have been added to controllably mimic the presence of the tech-grade impurities.²² In addition, TOPO has been replaced with various fatty acids, such as stearic and lauric acid, where shorter alkyl chain lengths yield relatively faster particle growth. The fatty-acid systems are compatible with the full range of cadmium precursors, but are most suited for the growth of larger NQDs (>6 nm in diameter), compared to the TOPO/TOP system, as growth proceeds quickly.²¹ For example, the cadmium precursor is typically dissolved in the fatty acid at moderate temperatures, converting the Cd compound into cadmium stearate. Alkyl amines were also successfully employed as CdSe growth media.²¹ Incompatible systems are those that contain the anion of a strong acid (present as the surfactant ligand or as the cadmium precursor) and thiol-based systems.²³ Perhaps the most successful system, in terms of producing high quantum yields (QYs) in emission and

monodisperse samples, uses a more complex mixture of surfactants: stearic acid, TOPO, hexadecylamine (HDA), TBP, and dioctylamine.²⁴

1.2.3 OPTIMIZING PHOTOLUMINESCENCE

High QYs are indicative of a well-passivated surface. NQD emission can suffer from the presence of unsaturated, “dangling” bonds at the particle surface that act as surface traps for charge carriers. Recombination of trapped carriers leads to a characteristic emission band (“deep-trap” emission) on the low-energy side of the “band-edge” photoluminescence (PL) band. Band-edge emission is associated with recombination of carriers in NQD interior quantized states. Coordinating ligands help to passivate surface trap sites, enhancing the relative intensity of band-edge emission compared to the deep-trap emission. The complex mixed-solvent system, described earlier, has been used to generate NQDs having QYs as high as 70%–80%. These remarkably high PL efficiencies are comparable to the best achieved by inorganic epitaxial-shell surface-passivation techniques (see Section 1.3). They are attributed to the presence of a primary amine ligand, as well as to the use of excess selenium in the precursor mixture (ratio Cd:Se of 1:10). The former alone (i.e., coupled with a “traditional” Cd:Se ratio of 2:1 or 1:1) yields PL QYs that are higher than those typically achieved by organic passivation (40%–50% compared to 5%–15%). The significance of the latter likely results from the unequal reactivities of the cadmium and selenium precursors. Accounting for the relative precursor reactivities using concentration-biased mixed precursors may permit improved crystalline growth and, hence, improved PL QYs.²⁴ Further, to achieve the very high QYs, reactions must be conducted over limited time span of 5–30 min. PL efficiencies reach a maximum in the first half of the reaction and decline thereafter. Optimized preparations yield rather large NQDs, emitting in the orange-red. However, high-QY NQDs representing a variety of particle sizes are possible. By controlling precursor identity, total precursor concentrations, the identity of the solvent system, the nucleation and growth temperatures, and the growth time, NQDs emitting with >30% efficiency from ~510 to 650 nm can be prepared.²⁴ Finally, the important influence of the primary amine ligands may result from their ability to pack more efficiently on the NQD surfaces. Compared to TOPO and TOP, primary amines are less sterically hindered and may simply allow for a higher capping density.²⁵ However, the amine-CdSe NQD linkage is not as stable as for other more strongly bound CdSe ligands.²⁶ Thus, growth solutions prepared from this procedure are highly luminescent but washing or processing into a new liquid or solid matrix can dramatically impact the QY. Multidentate amines may provide both the desired high PL efficiencies and the necessary chemical stabilities.²⁴

High-quality NQDs are no longer limited to cadmium-based II-VI compounds. Preparations for III-V semiconductor NQDs are well developed and are discussed in Chapter 9. Exclusively band-edge UV to blue emitting ZnSe NQDs ($\sigma = 10\%$) exhibiting QYs from 20% to 50% have been prepared by pyrolysis of diethylzinc and TOPSe at high temperatures (nucleation: 310°C; growth: 270°C). Successful reactions employed HDA/TOP as the solvent system (elemental analysis indicating that bound surface ligands comprised two-thirds HDA and one-third TOP), whereas the TOPO/TOP combination did not work for this material. Indeed, the nature of the reaction product was very sensitive to the TOPO/TOP ratio. Too much TOPO, which

binds strongly to Zn, generated particles so small that they could not be precipitated from solution by addition of a nonsolvent. Too much TOP, which binds very weakly to Zn, yielded particles that formed insoluble aggregates. As somewhat weaker bases compared to phosphine oxides, primary amines were chosen as ligands of intermediate strength, and may provide enhanced capping density (as discussed earlier).²⁵ HDA, in contrast with shorter-chain primary amines (octylamine and dodecylamine), provided good solubility properties and permitted sufficiently high growth temperatures for reasonably rapid growth of highly crystalline ZnSe NQDs.²⁵

High-quality NQDs absorbing and emitting in the infrared have also been prepared by way of a surfactant-stabilized pyrolysis reaction. PbSe colloidal QDs can be synthesized from the precursors: lead oleate (prepared *in situ* from lead(II)acetate trihydrate and oleic acid)²³ and TOPSe.^{10,23} TOP and oleic acid are present as the coordinating solvents, whereas phenyl ether, a non-coordinating solvent, provides the balance of the reaction solution. Injection and growth temperatures were varied (injection: 180°C–210°C; growth: 110°C–130°C) to control particle size from ~3.5 to ~9 nm in diameter.²³ The particles respond to “traditional” size-selection precipitation methods, allowing the narrow as-prepared size dispersions ($\sigma \leq 10\%$) to be further refined ($\sigma = 5\%$) (Figure 1.4).¹⁰ Oleic acid provides excellent capping properties as PL quantum efficiencies, relative to IR dye no. 26, can approach 100% (Figure 1.5).²³ Importantly, PbSe NQDs are substantially more efficient IR emitters than their organic-dye counterparts and provide enhanced photostability compared to existing IR fluorophores. More recently, a synthetic route to large-size PbSe NQDs (>8 nm) has been described that permits particle-size-tunable *mid-infrared* emission (>2.5 μm) with efficient, narrow-bandwidth emission at energies as low as 0.30 eV (4.1 μm).²⁷

1.2.4 AQUEOUS-BASED SYNTHETIC ROUTES AND THE INVERSE-MICELLE APPROACH

In addition to the moderate (~150°C) and high-temperature (>200°C) preparations discussed earlier, many room-temperature reactions have been developed. The two most prevalent schemes entail thiol-stabilized aqueous-phase growth and inverse-micelle methods.

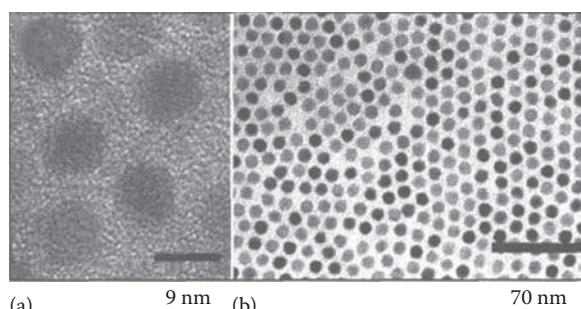


FIGURE 1.4 (a) HR TEM of PbSe NQDs, where the internal crystal lattice is evident for several of the particles. (b) Lower-magnification imaging reveals the nearly uniform size and shape of the PbSe NQDs. (Reprinted with permission from Murray, C. B. et al., *IBM J. Res. Dev.*, 45, 47, 2001.)

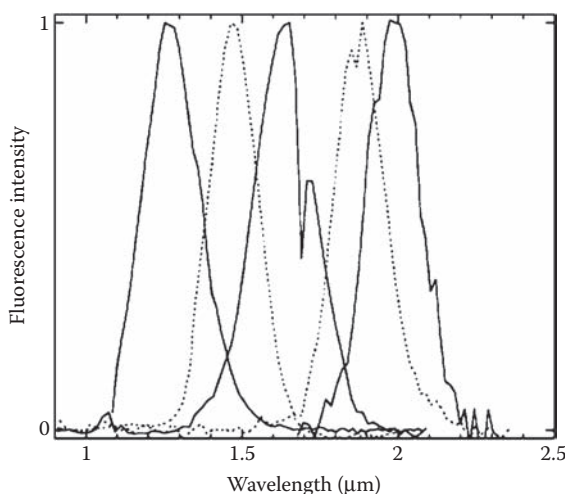


FIGURE 1.5 PbSe NQD size-dependent room-temperature fluorescence (excitation source: 1.064 μm laser pulse). Sharp features at \sim 1.7 and 1.85 μm correspond to solvent (chloroform) absorption. (Reprinted with permission from Wehrenberg, B. L., C. J. Wang, P. Guyot-Sionnest, *J. Phys. Chem. B*, 106, 10634, 2002.)

These approaches are discussed briefly here, and the former is discussed in some detail in Section 1.3 as it pertains to core/shell nanoparticle growth, whereas the latter is revisited in Section 1.6 with respect to its application to NQD doping. In general, the low-temperature methods suffer from relatively poor size dispersions ($\sigma > 20\%$) and often exhibit significant, if not exclusively, trap-state PL. The latter is inherently weak and broad compared to band-edge PL, and it is less sensitive to quantum-size effects and particle-size control. Further, low-T aqueous preparations have typically been limited in their applicability to relatively ionic materials. Higher temperatures are generally required to prepare *crystalline* covalent compounds (barring reaction conditions that may reduce the energetic barriers to crystalline growth, e.g., catalysts and templating structures). Thus, II-VI compounds, which are more ionic compared to III-V compounds, have been successfully prepared at low temperatures (room T or less), whereas attempts to prepare high-quality III-V compound semiconductors have been less successful.²⁸ Some relatively successful examples of low-T aqueous routes to III-V NQDs have been reported,²⁹ but particle quality is less than what has become customary for higher-T methods. Nevertheless, the mild reaction conditions afforded by aqueous-based preparations is a processing advantage.

The processes of nucleation and growth in aqueous systems are conceptually similar to those observed in their higher-temperature counterparts. Typically, the metal perchlorate salt is dissolved in water, and the thiol stabilizer is added (commonly, 1-thioglycerol). After the pH is adjusted to >11 (or from 5 to 6 if ligand is a mercaptoamine)³⁰ and the solution is deaerated, the chalcogenide is added as the hydrogen chalcogenide gas.^{28,31,32} Addition of the chalcogenide induces particle nucleation. The nucleation process appears not to be an ideal, temporally discrete event, as the initial particle-size dispersion is broad. Growth, or “ripening,” is allowed to

proceed over several days, after which a redshift in the PL spectrum is observed, and the spectrum is still broad.²⁸ For example, fractional precipitation of an aged CdTe growth solution yields a size series exhibiting emission spectra centered from 540 to 695 nm, where the full width at half maximum (FWHM) of the size-selected samples are at best 50 nm,²⁸ compared to ~20 nm for the best high-temperature reactions. In Cd-based systems, the ripening process can be accelerated by warming the solution; however, in the Hg-based systems heating the solution results in particle instability and degradation.²⁸ Initial particle size can be roughly tuned by changing the identity of the thiol ligand. The thiol binds to metal ions in solution before particle nucleation, and extended x-ray absorption fine structure (EXAFS) studies have demonstrated that the thiol stabilizer binds exclusively to metal surface sites in the formed particles.³³ By changing the strength of this metal–thiol interaction, larger or smaller particle sizes can be obtained. For example, decreasing the bond strength by introducing an electron withdrawing group adjacent to the sulfur atom leads to larger particles.^{30,33}

Another advantage of room-temperature, aqueous-based reactions lies in their ability to produce nanocrystal compositions that are less accessible by higher-temperature pyrolysis methods. Of the II–VI compounds, Hg-based materials are generally restricted to the temperature/ligand combination afforded by the aqueous thiol-stabilized preparations. The nucleation and growth of mercury chalcogenides have proven difficult to control in higher-temperature, nonaqueous reactions. Relatively weak ligands, fatty acids and amines (stability constant $K < 10^{17}$), yield fast growth and precipitation of the mercury chalcogenide, whereas stronger ligands, polyamines, phosphines, phosphine oxides, and thiols (stability constant $K > 10^{17}$), promote reductive elimination of metallic mercury at elevated temperatures.¹⁸ Very high PL efficiencies (up to 50%) are reported for HgTe NQDs prepared in water.³² However, the as-prepared samples yield approximately featureless absorption spectra and broad PL spectra. Further, the PL QYs for NQDs that emit at $> 1 \mu\text{m}$ have been determined in comparison with Rhodamine 6G, which has a PL maximum at ~550 nm. Typically, spectral overlap between the NQD emission signal and the reference organic dye is desired to better ensure reasonable QY values by taking into account the spectral response of the detector.

An alternative low-temperature approach that has been applied to a variety of systems, including mercury chalcogenides, is the inverse-micelle method. In general, the reversed-micelle approach entails preparation of a surfactant/polar-solvent/nonpolar-solvent microemulsion, where the content of the spontaneously generated spherical micelles is the polar-solvent fraction and that of the external matrix is the nonpolar solvent. The surfactant is commonly dioctyl sulfosuccinate, sodium salt (AOT). Precursor cations and anions are added and enter the polar phase. Precipitation follows, and particle size is controlled by the size of the inverse-micelle “nanoreactors,” as determined by the water content, W, where $W = [\text{H}_2\text{O}]/[\text{AOT}]$. For example, in an early preparation, AOT was mixed with water and heptane, forming the microemulsion. Cd^{2+} , as $\text{Cd}(\text{ClO}_4)_2 \cdot 6\text{H}_2\text{O}$, was stirred into the microemulsion allowing it to become incorporated into the interior of the reverse micelles. The selenium precursor was subsequently added and, upon mixing with cadmium, nucleated colloidal CdSe. Untreated solutions were observed to flocculate within hours, yielding insoluble aggregated nanoparticles. Addition of excess water quickened this

process. However, promptly evaporating the solutions to dryness, removing micellar water, yielded surfactant-encased colloids that could be redissolved in hydrocarbon solvents. Alternatively, surface passivation could be provided by first growing a cadmium shell via further addition of Cd²⁺ precursor to the microemulsion followed by addition of phenyl(trimethylsilyl)selenium (PhSeTMS). PhSe-surface passivation prompted precipitation of the colloids from the microemulsion. The colloids could then be collected by centrifugation or filtering and redissolved in pyridine.³⁴

Recently, the inverse-micelle technique has been applied to mercury-chalcogenides as a means to control the fast growth rates characteristic of this system (see preceding text).¹⁸ The process employed is similar to traditional micelle approaches; however, the metal and chalcogenide precursors are phase segregated. The mercury precursor (e.g., mercury(II)acetate) is transferred to the aqueous phase, while the sulfur precursor [bis (trimethylsilyl) sulfide, (TMS)₂S] is introduced to the nonpolar phase. Additional control over growth rates is provided by the strong mercury ligand, thioglycerol, similar to thiol-stabilized aqueous-based preparations. Growth is arrested by replacing the sulfur solution with aqueous or organometallic cadmium or zinc solutions. The Cd or Zn add to the surface of the growing particles and sufficiently alter surface reactivity to effectively halt growth. Interestingly, addition of the *organometallic* metal sources results in a significant increase in PL QY to 5%–6%, whereas no observable increase accompanies passivation with the aqueous sources. Wide size dispersions are reported ($\sigma = 20\%-30\%$). Nevertheless, absorption spectra are sufficiently well developed to clearly demonstrate that associated PL spectra, redshifted with respect to the absorption band edge, derive from band-edge luminescence and not deep-trap-state emission. Finally, ligand exchange with thiophenol permits isolation as aprotic polar-soluble NQDs, whereas exchange with long-chain thiols or amines permits isolation as nonpolar-soluble NQDs.¹⁸

The inverse-micelle approach may also offer a generalized scheme for the preparation of monodisperse metal-oxide nanoparticles.³⁵ The reported materials are ferroelectric oxides and, thus, stray from our emphasis on optically active semiconductor NQDs. Nevertheless, the method demonstrates an intriguing and useful approach: the combination of sol-gel techniques with inverse-micelle nanoparticle synthesis (with *moderate*-temperature nucleation and growth). Monodisperse barium titanate, BaTiO₃, nanocrystals, with diameters controlled in the range 6–12 nm, were prepared. In addition, proof-of-principle preparations were successfully conducted for TiO₂ and PbTiO₃. *Single-source* alkoxide precursors are used to ensure proper stoichiometry in the preparation of complex oxides (e.g., bimetallic oxides) and are commercially available for a variety of systems. The precursor is injected into a stabilizer-containing solvent (oleic acid in diphenyl ether; “moderate” injection temperature: 140°C). The hydrolysis-sensitive precursor is, up to this point, protected from water. The solution temperature is then reduced to 100°C (growth temperature), and 30wt% hydrogen peroxide solution (H₂O/H₂O₂) is added. Addition of the H₂O/H₂O₂ solution generates the microemulsion state and prompts a vigorous exothermic reaction. Control over particle size is exercised either by changing the precursor/stabilizer ratio or the amount of H₂O/H₂O₂ solution that is added. Increasing either results in an increased particle size, whereas decreasing the precursor/stabilizer ratio leads to a decrease in particle size. Following growth over 48 h, the particles are extracted into nonpolar solvents

such as hexane. By controlled evaporation from hexane, the BaTiO₃ nanocrystals can be self-assembled into ordered superlattices (SLs) exhibiting periodicity over several microns, confirming the high monodispersity of the sample (see Section 1.7).³⁵

1.3 INORGANIC SURFACE MODIFICATION

Surfaces play an increasing role in determining nanocrystal structural and optical properties as particle size is reduced. For example, due to an increasing surface-to-volume ratio with diminishing particle size, surface trap states exert an enhanced influence over PL properties, including emission efficiency, and spectral shape, position and dynamics. Further, it is often through their surfaces that semiconductor nanocrystals interact with their chemical environment, as soluble species in an organic solution, reactants in common organic reactions, polymerization centers, biological tags, electron/hole donors/acceptors, etc. Controlling inorganic and organic surface chemistry is key to controlling the physical and chemical properties that make NQDs unique compared to their epitaxial quantum-dot counterparts. The previous section discussed the impact of organic ligands on particle growth and particle properties. This section reviews surface modification techniques that utilize *inorganic* surface treatments.

1.3.1 (CORE)SHELL NQDs

Overcoating highly monodisperse CdSe with epitaxial layers of either ZnS^{36,37} or CdS (Figure 1.6)²⁵ has become routine and typically provides almost an order of magnitude enhancement in PL efficiency compared to the exclusively organic-capped starting nanocrystals (e.g., 5%–10% efficiencies can yield 30%–70% efficiencies [Figure 1.7]). The enhanced quantum efficiencies result from enhanced coordination of surface unsaturated, or dangling, bonds, as well as from increased confinement of electrons and holes to the particle core. The latter effect occurs when the band gap of the shell material is larger than that of the core material, as is the case for (CdSe)ZnS and (CdSe)CdS (core)shell particles. Successful overcoating of III-V semiconductors has also been reported^{38–40}.

The various preparations share several synthetic features. First, the best results are achieved if initial particle size distributions are narrow, as some size-distribution broadening occurs during the shell-growth process. Because absorption spectra are relatively unchanged by surface properties, they can be used to monitor the stability of the nanocrystal core during and following growth of the inorganic shell. Further, if the conduction band offset between the core and the shell materials is sufficiently large (i.e., large compared to the electron confinement energy), then significant redshifting of the absorption band edge should not occur, as the electron wave function remains confined to the core (Figure 1.8). A large redshift in (core)shell systems, having sufficiently large offsets (determined by the identity of the core/shell materials and the electron and hole effective masses), indicates growth of the core particles during shell preparation. A small broadening of absorption features is common and results from some broadening of the particle size dispersion (Figure 1.8). Alloying, or mixing of the shell components into the interior of the core, would also be evident in absorption spectra if it were to occur. The band edge would shift to some intermediate

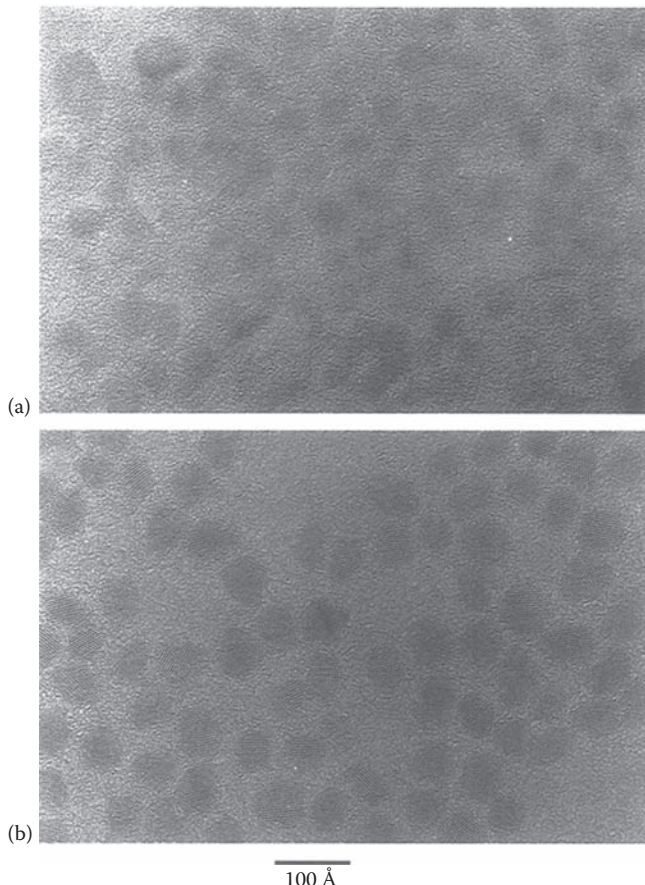


FIGURE 1.6 Wide-field HR-TEMs of (a) 3.4 nm diameter CdSe core particles and (b) (CdSe)CdS (core)shell particles prepared from the core NQDs in (a) by overcoating with a 0.9 nm thick CdS shell. Where lattice fringes are evident, they span the entire nanocrystal, indicating epitaxial (core)shell growth. (Reprinted with permission from Peng, X., M. C. Schlamp, A. V. Kadavanich, and A.P. Alivisatos, *J. Am. Chem. Soc.*, 119, 7019, 1997.)

energy between the band energies of the respective materials comprising the alloyed nanoparticle.

PL spectra can be used to indicate whether effective passivation of surface traps has been achieved. In poorly passivated nanocrystals, deep-trap emission is evident as a broad tail or hump to the red of the sharper band-edge emission spectral signal. The broad, trap signal will disappear and the sharp, band-edge luminescence will increase following successful shell growth ([Figure 1.7a](#)).

Note: The trap-state emission signal contribution is typically larger in smaller (higher relative-surface-area) nanocrystals than in larger nanoparticles ([Figure 1.7a](#)).

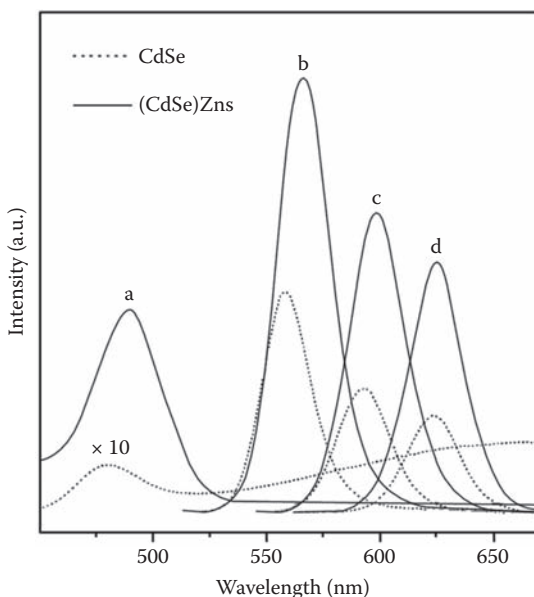


FIGURE 1.7 PL spectra for CdSe NQDs and (CdSe)ZnS (core)shell NQDs. Core diameters are (a) 2.3, (b) 4.2, (c) 4.8, and (d) 5.5 nm. (Core)shell PL QYs are (a) 40, (b) 50, (c) 35, and (d) 30%. Trap-state emission is evident in the (a) core-particle PL spectrum as a broad band to the red of the band-edge emission and absent in the respective (core)shell spectrum. (Reprinted with permission from Dabbousi, B. O., J. Rodriguez-Viejo, F. V. Mikulec, J. R. Heine, H. Mattoussi, R. Ober, K. F. Jensen, and M. G. Bawendi, *J. Phys. Chem. B*, 101, 9463, 1997.)

Homogeneous nucleation and growth of shell-material as discrete nanoparticles may compete with *heterogeneous* nucleation and growth at core-particle surfaces. Typically, a combination of relatively low precursor concentrations and reaction temperatures is used to avoid particle formation. Low precursor concentrations support undersaturated-solution conditions and, thereby, shell growth by *heterogeneous* nucleation. The precursors, diethylzinc and bis(trimethylsilyl) sulfide in the case of ZnS shell growth, for example, are added dropwise at relatively low temperatures to prevent buildup and supersaturation of unreacted precursor monomers in the growth solution. Further, employing relatively low reaction temperatures avoids growth of the starting core particles.^{26,37} ZnS, for example, can nucleate and grow as a crystalline shell at temperatures as low as 140°C³⁷, and CdS shells have been successfully prepared from dimethylcadmium and bis(trimethylsilyl) sulfide at 100°C²⁶, thereby avoiding complications due to homogeneous nucleation and core-particle growth. Additional strategies for preventing particle growth of the shell material include using organic capping ligands that have a particularly high affinity for the shell metal. The presence of a strong binding agent seems to lead to more controlled shell growth, for example, TOP is replaced with TOP in CdSe shell growth on InAs cores, where TOP (softer Lewis base) coordinates

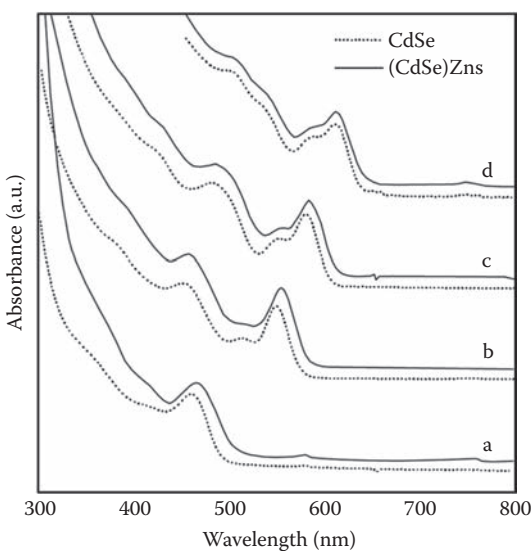


FIGURE 1.8 Absorption spectra for bare (dashed lines) and 1–2 monolayer ZnS-overcoated (solid lines) CdSe NQDs. (Core)shell spectra are broader and slightly redshifted compared to the core counterparts. Core diameters are (a) 2.3, (b) 4.2, (c) 4.8, and (d) 5.5 nm. (Reprinted with permission from Dabbousi, B. O., J. Rodriguez-Viejo, F. V. Mikulec, J. R. Heine, H. Mattoussi, R. Ober, K. F. Jensen, and M. G. Bawendi, *J. Phys. Chem. B*, 101, 9463, 1997.)

more tightly than TOPO (harder Lewis base) with cadmium (softer Lewis acid).⁴⁰ Finally, the ratio of the cationic to anionic precursors can be used to prevent shell-material homogeneous nucleation. For example, increasing the concentration of the chalcogenide in a cadmium-sulfur precursor mixture hinders formation of unwanted CdS particles.²⁶

Successful overcoating is possible for systems where relatively large lattice mismatches between core and shell crystal structures exist. The most commonly studied (core)shell system, (CdSe)ZnS, is successful despite a 12% lattice mismatch. Such a large lattice mismatch could not be tolerated in flat heterostructures, where strain-induced defects would dominate the interface. It is likely that the highly curved surface and reduced facet lengths of nanocrystals relax the structural requirements for epitaxy. Indeed, two types of epitaxial growth are evident in the (CdSe)ZnS system: coherent (with large distortion or strain) and incoherent (with dislocations), the difference arising for thin (~1–2 monolayers, where a monolayer is defined as 3.1 Å) versus thick (>2 monolayers) shells, respectively.³⁷ High-resolution (HR) TEM images of thin-shell-ZnS-overcoated CdSe QDs reveal lattice fringes that are continuous across the entire particle, with only a small “bending” of the lattice fringes in some particles indicating strain. TEM imaging has also revealed that thicker shells (>2 monolayers) lead to the formation of deformed particles, resulting from uneven growth across the particle surface. Here, too, however, the shell appeared epitaxial, oriented with the lattice of the core ([Figure 1.9](#)). Nevertheless, wide-angle x-ray

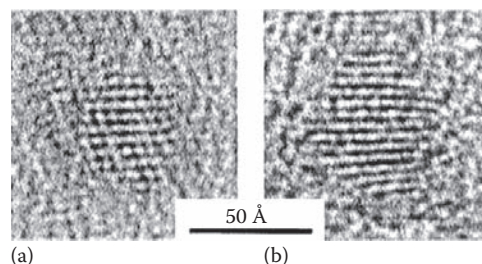


FIGURE 1.9 HR-TEM of (a) CdSe core particle and (b) a (CdSe)ZnS (core)shell particle (2.6 monolayer ZnS shell). Lattice fringes in (b) are continuous throughout the particle, suggesting epitaxial (core)shell growth. (Reprinted with permission from Dabbousi, B. O., J. Rodriguez-Viejo, F. V. Mikulec, J. R. Heine, H. Mattoussi, R. Ober, K. F. Jensen, and M. G. Bawendi, *J. Phys. Chem. B*, 101, 9463, 1997.)

scattering (WAXS) data showed reflections for both CdSe and ZnS, indicating that each was exhibiting its own lattice parameter in the thicker-shell systems. This type of structural relationship between the core and the shell was described as *incoherent* epitaxy. It was speculated that at low coverage, the epitaxy is coherent (strain is tolerated), but at higher coverages, the high lattice mismatch can no longer be sustained without the formation of dislocations and low-angle grain boundaries. Such defects in the core–shell boundary provide nonradiative recombination sites and lead to diminished PL efficiency compared to coherently epitaxial thinner shells. Further, in all cases studied where more than a single monolayer of ZnS was deposited, the shell appeared to be continuous. X-ray photoelectron spectroscopy (XPS) was used to detect the formation of SeO_2 following exposure to air. The SeO_2 peak was observed only in bare TOPO/TOP-capped dots and dots having less than one monolayer of ZnS overcoating. Together, the HR TEM images and XPS data suggest complete, epitaxial shell formation in the highly lattice-mismatched system of (CdSe)ZnS.

The effect of lattice mismatch has also been studied in III-V semiconductor core systems. Specifically, InAs has been successfully overcoated with InP, CdSe, ZnS, and ZnSe.⁴⁰ The degree of lattice mismatch between InAs and the various shell materials differed considerably, as did the PL efficiencies achieved for these systems. However, no direct correlation between lattice mismatch and QY in PL was observed. For example, (InAs)InP produced quenched luminescence whereas (InAs)ZnSe provided up to 20% PL QYs, where the respective lattice mismatches are 3.13% and 6.44%. CdSe shells, providing a lattice *match* for the InAs cores, also produced up to 20% PL QYs. In all cases, shell growth beyond two monolayers (where a monolayer equals the d_{111} lattice spacing of the shell material) caused a decrease in PL efficiencies, likely due to the formation of defects that could provide trap sites for charge carriers (as observed in (CdSe)ZnS³⁷ and (CdSe)CdS²⁶ systems). The perfectly lattice-matched CdSe shell material should provide the means for avoiding defect formation; however, the stable crystal structures for CdSe and InAs are different under the growth conditions employed. CdSe prefers the wurtzite structure while InAs prefers cubic. For this reason, it was thought that this “matched” system may succumb to interfacial defect formation with thick shell growth.⁴⁰

The larger contributor to PL efficiency in the (InAs)shell systems was found to be the size of the energy offset between the respective conduction and valence bands of the core and shell materials. Larger offsets provide larger potential energy barriers for the electron and hole wave functions at the (core)shell interface. For InP and CdSe, the conduction band offset with respect to InAs is small. This allows the electron wave function to “sample” the surface of the nanoparticle. In the case of CdSe, fairly high PL efficiencies can still be achieved because native trap sites are less prevalent than they are on InP surfaces. Both ZnS and ZnSe provide large energy offsets. The fact that the electron wave function remains confined to the core of the (core)shell particle is evident in the absorption and PL spectra. In these confined cases, no redshifting was observed in the optical spectra following shell growth.⁴⁰ The observation that PL enhancement to only 8% QY was possible using ZnS as the shell material may have been due to the large lattice mismatch between InAs and ZnS of ~11%. Otherwise, ZnS and ZnSe should behave similarly as shells for InAs cores.

Shell chemistry can be precisely controlled to achieve unstrained (core)shell epitaxy. For example, the zinc-cadmium alloy, ZnCdSe₂, was used for the preparation of (InP)ZnCdSe₂ nanoparticles having essentially zero lattice mismatch between the core and the shell.³⁸ HR TEM images demonstrated the epitaxial relationship between the layers, and very thick epilayer shells were grown—up to 10 monolayers—where a monolayer was defined as 5 Å. The shell layer successfully protected the InP surface from oxidation, a degradation process to which InP is particularly susceptible (see Chapter 9).

More recently, (core)shell growth techniques have been further refined to allow for precise control over shell thickness and shell monolayer additions. A technique developed originally for the deposition of thin-films onto solid substrates—successive ion layer adsorption and reaction (SILAR)—was adapted for NQD shell growth.⁴¹ Here, homogenous nucleation of the shell composition is largely avoided and higher shell-growth temperatures are tolerated because the cationic and anionic species do not coexist in the growth solution. This method has allowed for growth of thick shells, comprising many shell monolayers, without loss of NQD size monodispersity and with superior shell crystalline quality. Originally demonstrated for a single-composition shell (CdS over CdSe) up to five monolayers thick,⁴¹ the approach has been extended to multishell architectures,^{42,43} as well as to “ultrathick” shell systems (>10 monolayers) (see Section 1.3.2).⁴³ The multishell architectures [e.g., (CdS)Zn_{0.5}Cd_{0.5}S/ZnS] provide for a “stepwise” tuning of the shell composition, and, thereby, tuning of the lattice parameters and the valence- and conduction-band offsets in the radial direction. The resulting nanocrystals are highly crystalline, uniform in shape, and electronically well passivated.⁴²

For some NQD core materials, traditional (core)shell reaction conditions are too harsh and result in diminished integrity of the starting core material. This loss in NQD core integrity is manifested as uncontrolled particle growth by way of Ostwald ripening, as well as by unpredictable shifts in absorption onsets and, often, decreases in PL intensity. For example, the inability to reliably grow functional shells onto lead chalcogenide NQDs, such as PbSe and PbS, using the conventional paradigm for (core)shell NQD synthesis—in which a solution of NQD cores is exposed at elevated temperatures to precursors comprising both the anion and cation of the shell material—led to

the development of a novel shell growth method based on “partial cation exchange.”⁴⁴ Here, the NQD cores are exposed only to a precursor that contains the desired shell’s cation, and the reaction is conducted at room temperature to moderate temperatures to avoid uncontrolled ripening of the core NQDs. Over time, the shell cation (e.g., cadmium) reacts with the lead-based NQDs at their surfaces to replace a fraction of the lead in the original NQD. The fraction of lead that is replaced is determined by the reaction time, the reaction temperature, and the amount of excess shell-cation precursor that is supplied to the reaction. In contrast with cation-exchange approaches for which the primary aim is *complete* exchange of cations,⁴⁵ highly ionic and reactive precursors, as well as strong cation-binding solvents, are expressly avoided. Instead, use of a relatively slow-reacting cadmium precursor, soluble in non-coordinating solvents, allows a more subtle shift in the solution equilibrium toward net ion substitution that can be controlled easily by changing reaction parameters. Ultimately, ~5%–75% of the original lead in the NQD core can be replaced resulting in a range of shell thicknesses. The process takes advantage of the large lability of the lead chalcogenide NQDs, and has been used to controllably synthesize (PbSe)CdSe and (PbS)CdS core/shell NQDs.⁴⁴ The resulting (core)shell NQDs are more stable against oxidation and Ostwald ripening processes, and they exhibit enhanced emission efficiencies compared to the starting core materials. Interestingly, as a result of their enhanced chemical stability, they are amenable to secondary shell growth, such as ZnS onto (PbSe)CdSe, using *traditional* growth techniques.⁴⁴

1.3.2 GIANT-SHELL NQDs

The first all-inorganic approach to suppression of “blinking” or fluorescence intermittency in NQDs was recently reported, where addition of “giant” (thick), wider band-gap semiconductor shells to the emitting NQD core was found to render the new (core)shell NQD substantially nonblinking.⁴³ Previously, only organic surface-ligand approaches had been used successfully,^{46–48} though questions remained regarding the environmental and temporal robustness of an organic approach.⁴⁹ Interestingly, the inorganic shell approach was initially thought not to be effective at suppressing blinking.⁵⁰ However, when inorganic shell growth is executed with extreme precision and shells are of sufficient thickness, a functionally new NQD structural regime is achieved for which blinking, as well as other key optical properties, are fundamentally altered. Specifically, the very thick, wider band-gap semiconductor shell is thought to provide near-complete isolation of the NQD core wavefunction from the NQD surface and surface environment. In this way, the “giant-shell” NQD architecture is structurally more akin to physically grown epitaxial QDs, for which optical properties are stable and blinking is not observed.⁵¹

The ultrathick shells (~8–20 monolayers) were grown onto CdSe NQD cores using a modified SILAR approach (Figure 1.10).⁴³ The shell was either single-component (e.g., (CdSe)₁₉CdS NQDs [Figure 1.10b; 15.5 ± 3.1 nm]) or multicomponent (e.g., (CdSe)₁₁CdS_xZn_yS-2ZnS [Figure 1.10c; 18.3 ± 2.9 nm]), where the 6 layers of alloyed shell material (6Cd_xZn_yS) were successively richer in Zn (from nominally 0.13 to 0.80 atomic% Zn). The blinking statistics were found to be similar for both the single- and multicomponent systems; however, the ensemble QYs in emission

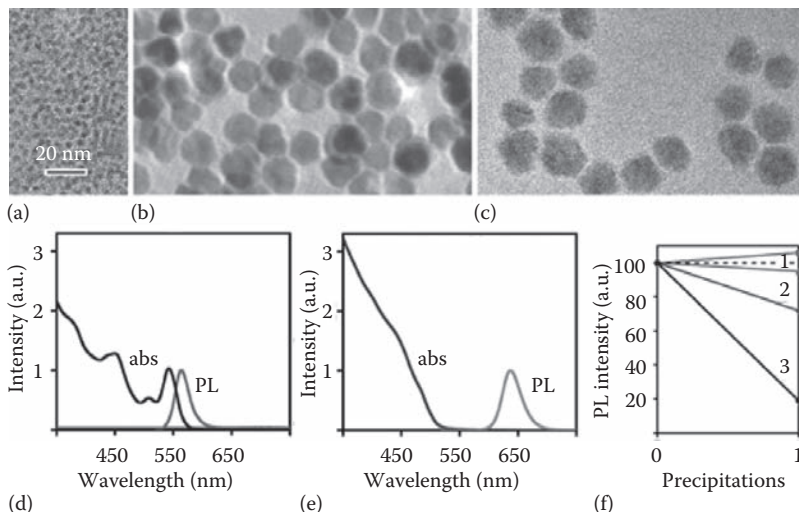


FIGURE 1.10 Low-resolution transmission electron microscopy (TEM) images for (a) CdSe NQD cores, (b) (CdSe)19CdS giant-shell NQDs, and (c) (CdSe)11CdS-6Cd_xZn_yS-2ZnS giant-shell NQDs. (d) Absorption (dark gray) and PL (light gray) spectra for CdSe NQD cores. (e) Absorption (dark gray) and PL (light gray) spectra for (CdSe)19CdS giant-shell NQDs (inset: absorption spectrum expanded to show contribution from core). (f) Normalized PL compared for growth solution and first precipitation/redissolution for (CdSe)11CdS-6Cd_xZn_yS-2ZnS and (CdSe)19CdS giant-shell NQDs (1), (CdSe)2CdS-2ZnS and (CdSe)2CdS-3Cd_xZn_yS-2ZnS NQDs (2), and CdSe core NQDs (3). Dashed line indicates no change. (Adapted from Chen, Y., J. Vela, H. Htoon, J. L. Casson, D. J. Werder, D. A. Bussian, V. I. Klimov, and J. A. Hollingsworth, *J. Am. Chem. Soc.*, 130, 5026, 2008.)

were observed to be superior for the single-component system.⁴³ The ability of the all-CdS giant-shell motif to reliably afford suppressed blinking for CdSe NQD cores was confirmed by a subsequent independent report.⁵² Despite long growth times (typically several days), reasonable control over size dispersity ([Figure 1.10b and c](#)) can be maintained ($\pm 15\%-20\%$), along with retention of a regular, faceted particle shape ([Figure 1.11](#)). Compared to conventional NQDs, the giant-shell NQDs are characterized by a large effective Stokes shift, as the absorption spectra are dominated by the shell material, while the emission is from the CdSe core ([Figure 1.10d and e](#)). This is not surprising, as the shell:core volume ratio can approach 100:1 in the thickest-shell examples. Significantly, energy transfer from the thick, wider-gap shell to the emitting core is efficient, enhancing the NQD absorption cross-section and preventing PL from the shell. Further, giant-shell NQDs were observed to be uniquely insensitive to changes in ligand concentration and identity, and the chemical stability afforded by these NQDs was found to clearly surpass that of the standard multishell and core-only NQDs ([Figure 1.10f](#)).⁴³

Perhaps most remarkably, the giant-shell NQDs are characterized by substantially altered photobleaching and blinking behavior compared to conventional NQDs. Specifically, freshly diluted giant-shell NQDs when dispersed from either a nonpolar

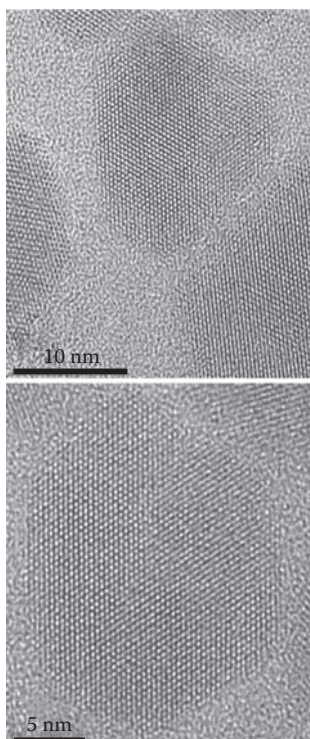


FIGURE 1.11 HR TEM images for (CdSe)19CdS giant-shell NQDs. (Adapted from Chen, Y., J. Vela, H. Htoon, J. L. Casson, D. J. Werder, D. A. Bussian, V. I. Klimov, and J. A. Hollingsworth, *J. Am. Chem. Soc.*, 130, 5026, 2008.)

solvent or from water onto clean quartz slides are not observed to photobleach under continuous laser illumination for several hours at a time over periods of several days. This result stands in stark contrast with those obtained for conventional NQD samples. Namely, core-only samples photobleach (complete absence of PL) within 1 s, and conventional (core)shell NDQs photobleach with a $t^{1/2} \sim 15$ min.⁴³ Moreover, under such continuous excitation conditions, significantly suppressed blinking behavior has been reported for giant-shell NQDs possessing $\sim 8^{52}$ and more⁴³ shell monolayers. For example, $\sim 45\%$ of a (core)shell NQD sample comprising a CdSe core and a 16-monolayer CdS shell was observed to be “on” (bright) 99% or more of the total observation time—a notable 54 min, while $\sim 65\%$ of the sample was found to be “on” 80% or more of the time (Figure 1.12a). In contrast, and typical of classically blinking NQDs, the majority ($\sim 70\%-90\%$) of a conventional (core)/shell NQD sample, for example, commercial Qdot®655ITK™ NQDs or even 5-monolayer-shell (CdSe)CdS NQDs, was observed to be on for only 20% or less of the observation time.^{43,53} Such long-observation-time data are collected with a temporal resolution of 200 ms, but it can also be shown that giant-shell NQDs exhibit nonblinking behavior even as short timescales using a time-correlated single-photon-counting technique (Figure 1.12b).

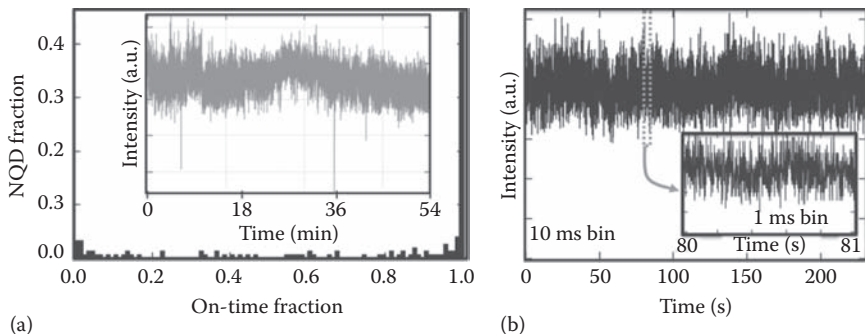


FIGURE 1.12 (a) On-time histogram of $(\text{CdSe})_{19}\text{CdS}$ giant-shell NQDs. Temporal resolution is 200 ms. Inset shows fluorescence time-trace for a representative NQD. (Adapted from Hollingsworth, J. A. et al., unpublished.) (b) Blinking data obtained using a time-correlated-single-photon-counting technique showing blinking behavior at timescales down to 1 ms. For nonblinking giant-shell NQDs, no blinking was observed at these faster timescales for the complete observation time of almost 4 min. (Adapted from Htoon, H. et al., unpublished.)

Finally, in the case of conventional NQDs, the probability density of on/off time distributions decay follows a power law $P(\tau) \propto \tau^{-m}$ with $m \sim 1.5$. Typically, m of the “on-time” distribution is larger than that of the “off-time” distribution, and it exhibits near-exponential fall-off at longer timescales. This is evident, for example, for $(\text{CdSe})\text{CdS}$ (core)shell NQDs comprising five shell monolayers (Figure 1.13a and c). However, giant-shell NQDs (where the CdS shell comprises 16 monolayers) that are characterized by total on-time fractions of $\geq 75\%$ (shaded region in Figure 1.13b) show nearly opposite behavior. Intriguingly, while the “off-time” distribution decays much more rapidly with $m \sim 3.0$, the decay of the “on-time” distribution is much slower and exhibits non-power-law decay (Figure 1.13d).

1.3.3 QUANTUM-DOT/QUANTUM-WELL STRUCTURES

Optoelectronic devices comprising two-dimensional (2-D) quantum-well (QW) structures are generally limited to material pairs that are well lattice-matched due to the limited strain tolerance of such planar systems; otherwise, very thin well layers are required. To access additional QW-type structures, more strain-tolerant systems must be employed. As already alluded to, the highly curved quantum dot nanostructure is ideal for lattice mismatched systems. Several QD/QW structures have been successfully synthesized, ranging from the well lattice matched $\text{CdS}(\text{HgS})\text{CdS}$ ^{54–56} (QD, QW, cladding) to the more highly strained $\text{ZnS}(\text{CdS})\text{ZnS}$.⁵⁷ The former provides emission color tunability in the infrared spectral region, while the latter yields access to the blue-green spectral region. In contrast to the very successful (core) shell preparations discussed earlier in this section, the QD/QW structures have been prepared using ion displacement reactions, rather than heterogeneous nucleation on the core surface (Figure 1.14). These preparations have been either aqueous or polar-solvent based and conducted at low temperatures (room temperature to -77°C).

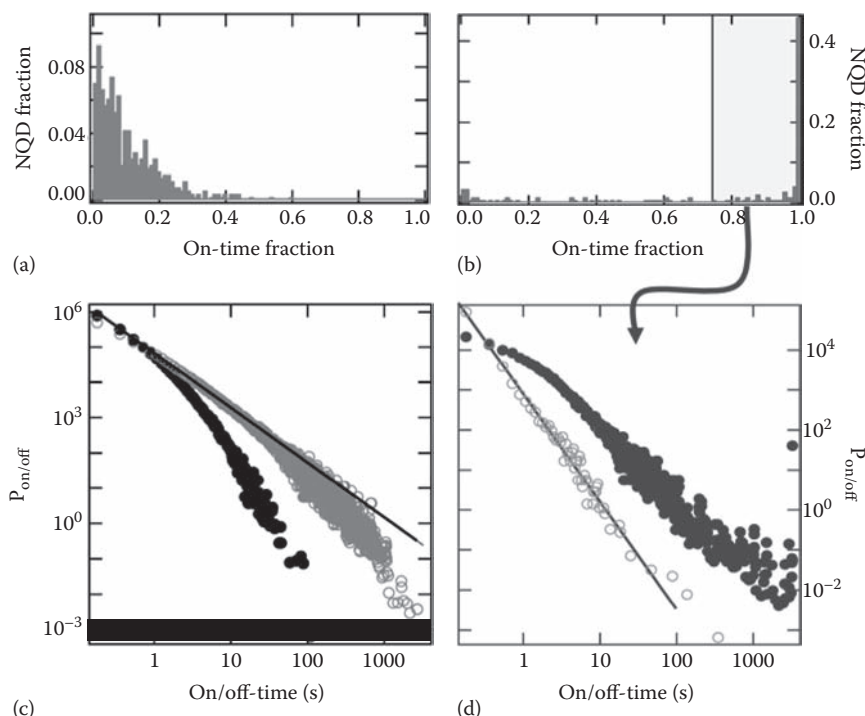


FIGURE 1.13 Histograms showing the distribution of on-time fractions for (a) conventional NQDs and (b) giant-shell NQDs coated by a shell comprising 16 monolayers of CdS. While more than 90% of the conventional NQDs have an on-time fraction less than 25%, more than 80% of the giant-shell NQDs have an on-time fraction larger than 75%. Distribution of “on-time” (black solid circles) and “off-time” intervals (open gray circles) for (c) conventional NQDs and (d) giant-shell NQDs. Off-time interval distributions of conventional NQDs exhibit a well-known power law behavior [$P \propto \tau^{-m}$], where $m \sim 1.5$. The on-time distribution also decays with a similar power law and falls off exponentially at longer times (>1 s). In contrast, off-time interval distributions of giant-shell NQDs with on-time fractions $>75\%$ (shaded region in [b]) exhibit a power law decay with a significantly larger “ m ” value (~ 2.00 – 3.00). Further, on-time interval distributions cannot be described by a simple power law. (Adapted from Htoon, H. et al., unpublished.)

They entail a series of steps that first involves the preparation of the nanocrystal cores (CdS and ZnS, respectively). Core preparation is followed by ion exchange reactions in which a salt precursor of the “well” metal ion is added to the solution of “core” particles. The solubility product constant (K_{sp}) of the metal sulfide corresponding to the added metal species is such that it is significantly less than that of the metal sulfide of the core metal species. This solubility relationship leads to precipitation of the added metal ions and dissolution of the surface layer of core metal ions via ion exchange. Analysis of absorption spectra during addition of “well” ions to the nanoparticle solution revealed an apparent concentration threshold, after which addition of the “well” ions produced no more change in the optical spectra.

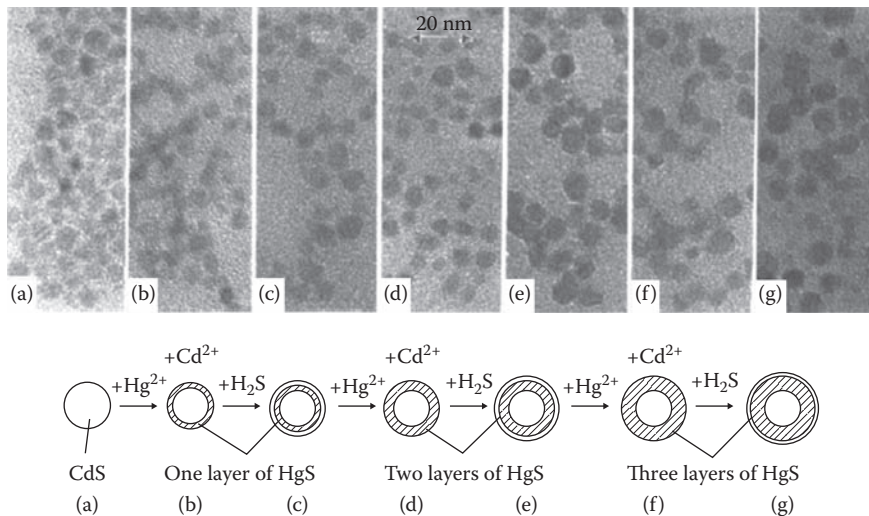


FIGURE 1.14 TEMs of CdS(HgS)CdS at various stages of the ion displacement process, where the latter is schematically represented in the figure. (Reprinted with permission from Mews, A., A. Eychmüller, M. Giersig, D. Schoos, and H. Weller, *J. Phys. Chem.*, 98, 934, 1994.)

Specifically, in the case of the CdS(HgS)CdS system, ion exchange of Hg^{2+} for Cd^{2+} produced a redshift in absorption until a certain amount of “well” ions had been added. According to inductively coupled plasma-mass spectrometry (ICP-MS), which was used to measure the concentration of free ions in solution for both species, up until this threshold concentration was reached, the concentration of free Hg^{2+} ions was essentially zero, while the Cd^{2+} concentration increased linearly. After the threshold concentration was reached, the Hg^{2+} concentration increased linearly (with each externally provided addition to the system), while the Cd^{2+} concentration remained approximately steady. These results agree well with the ion exchange reaction scenario, and, perhaps more importantly, suggest a certain natural limit to the exchange process. It was determined that in the example of 5.3 nm CdS starting core nanoparticles, approximately 40% of the Cd^{2+} was replaced with Hg^{2+} . This value agrees well with the conclusion that one complete monolayer has been replaced, as the surface-to-volume ratio in such nanoparticles is 0.42. Further dissolution of Cd^{2+} core ions is prevented by formation of the complete monolayer-thick shell, which also precludes the possibility of island-type shell growth.⁵⁵

Subsequent addition of H_2S or Na_2S causes the precipitation of the off-cast core ions back onto the particles. The ion replacement process, requiring the sacrifice of the newly redeposited core metal ions, can then be repeated to increase the thickness of the “well” layer. This process has been successfully repeated for up to three layers of well material. The “well” is then capped with a redeposited layer of core metal ions to generate the full QD/QW structure. The thickness of the cladding layer could be increased by addition in several steps (up to 5) of the metal and sulfur precursors.⁵⁵

The nature of the QD/QW structure and its crystalline quality have been analyzed by HR TEM. In the CdS(HgS)CdS system, evidence has been presented for both approximately spherical particles, as well as faceted particle shapes such as tetrahedrons and twinned tetrahedrons. In all cases, well and cladding growth is epitaxial as evidenced by the absence of amorphous regions in the nanocrystals and in the smooth continuation of lattice fringes across particles. Analysis of HR-TEM micrographs also reveals that the tetrahedral shapes are terminated by (111) surfaces that can be *either* cadmium or sulfur faces.⁵⁶ The choice of stabilizing agent—an anionic polyphosphate ligand—favors cadmium faces and likely supports the faceted tetrahedral structure that exposes exclusively cadmium-dominated surfaces (Figure 1.15). In addition, both the spherical particles and the twinned tetrahedral particles provide evidence for an embedded HgS layer in the presumed QD/QW structure. Owing to the differences in their relative abilities to interact with electrons (HgS more strongly than CdS), contrast differences are evident in HR-TEM images as bands of HgS surrounded by layers of CdS (Figure 1.15).

Size dispersions in these low-temperature, ionic-ligand stabilized reactions are reasonably good (~20%), as indicated by absorption spectra, but poor compared to those achieved using higher-temperature pyrolysis and amphiphilic coordinating

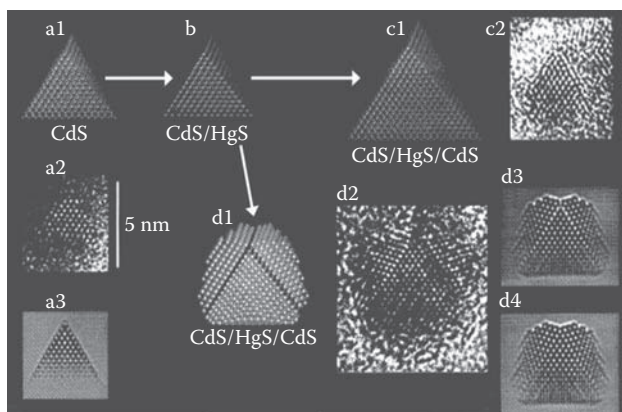


FIGURE 1.15 HR-TEM study of the structural evolution of a CdS core particle to a (CdS) (core)shell particle to the final CdS(HgS)CdS nanostructure. (a1) molecular model showing that all surfaces are cadmium terminated (111). (a2) TEM of a CdS core that exhibits tetrahedral morphology. (a3) TEM simulation agreeing with (a2) micrograph. (b) Model of the CdS particle after surface modification with Hg. (c1) Model of a tetrahedral CdS(HgS)CdS nanocrystal. (c2) A typical TEM of a tetrahedral CdS(HgS)CdS nanocrystal. (d1) Model of a CdS(HgS)CdS nanocrystal after twinned epitaxial growth, where the arrow indicates the interfacial layer exhibiting increased contrast due to the presence of HgS. (d2) TEM of a CdS(HgS)CdS nanocrystal after twinned epitaxial growth. (d3) Simulation agreeing with model (d1) and TEM (d2) showing increased contrast due to presence of HgS. (d4) Simulation assuming all Hg is replaced by Cd—no contrast is evident. (Reprinted with permission from Mews, A., A. V. Kadavanich, U. Banin, and A.P. Alivisatos, *Phys. Rev. B*, 53, R13242, 1996.)

ligands (4%–7%). Nevertheless, the polar-solvent-based reactions give us access to colloidal materials, such as mercury chalcogenides, thus far difficult to prepare using pyrolysis-driven reactions (Section 1.2). Further, the ion exchange method provides the ability to grow well and shell structures that appear to be precisely 1, 2, or 3 monolayers deep. Heterogeneous nucleation provides less control over shell thicknesses, resulting in incomplete and variable multilayers (e.g., 1.3 or 2.7 monolayers on average). Stability of core/shell materials against solid-state alloying is an issue, at least for the CdS(HgS)CdS system. Specifically, cadmium in a CdS/HgS structure will, within minutes, diffuse to the surface of the nanoparticle where it is subsequently replaced by a Hg²⁺ solvated ion.⁵⁵ This process is likely supported by the substantially greater aqueous solubility of Cd²⁺ compared to Hg²⁺, as well as the structural compatibility between the two lattice-matched CdS and HgS crystal structures.

1.3.4 TYPE-II AND QUASI-TYPE-II (CORE)SHELL NQDs

The (core)shell NQDs discussed in Section 1.3.1 comprise a shell material that has a substantially larger band gap than the core material. Further, the conduction and the valence band edges of the core semiconductor are located within the energy gap of the shell semiconductor. In this approach, the electron and hole experience a confinement potential that tends to localize both of the carriers in the NQD core, reducing their interactions with surface trap states and enhancing QYs in emission. This is referred to as type-I localization. Alternatively, (core)shell configurations can be such that the lowest energy states for electrons and holes are in different semiconductors. In this case, the energy gradient existing at the interfaces tends to spatially separate electrons and holes between the core and the shell. The corresponding “spatially indirect” energy gap (E_{g12}) is determined by the energy separation between the conduction-band edge of one semiconductor and the valence-band edge of the other semiconductor. This is referred to as type-II localization. Recent demonstrations of type-II colloidal core/shell NQDs include combinations of materials such as (CdTe)CdSe,⁵⁸ (CdSe)ZnTe,⁵⁸ (CdTe)CdS,⁵⁹ (CdTe)CdSe,⁶⁰ (ZnTe)CdS,⁶¹ and (ZnTe)CdTe,⁶¹ as well as non-Te-containing structures such as (ZnSe)CdSe⁶² and (CdS)ZnSe⁶³. The (ZnSe)CdSe NQDs are more precisely termed “quasi-type-II” structures, as they are only able to provide partial spatial separation between electrons and holes. In contrast, the (CdS)ZnSe NQD system provides for nearly complete spatial separation of electrons and holes with reasonably thin shells; and alloying the interface with a small amount of CdSe was shown to dramatically improve QYs in emission of these explicitly type-II structures.⁶³

1.4 SHAPE CONTROL

The nanoparticle growth process described in Section 1.2, where fast nucleation is followed by slower growth, leads to the formation of spherical or approximately spherical particles. Such essentially isotropic particles represent the thermodynamic, lowest energy, shape for materials having relatively isotropic underlying crystal structures. For example, under this growth regime, the wurtzite crystal structure of CdSe,

having a c/a ratio of ~1.6, fosters the growth of slightly prolate particles, typically exhibiting aspect ratios of ~1.2. Furthermore, even for materials whose underlying crystal structure is more highly anisotropic, nearly spherical nanoparticles typically result due to the strong influence of the surface in the nanosize regime. Surface energy is minimized in spherical particles compared to more anisotropic morphologies.

1.4.1 KINETICALLY DRIVEN GROWTH OF ANISOTROPIC NQD SHAPES: CdSe AS THE MODEL SYSTEM

Under a different growth regime, one that promotes fast, kinetic growth, more highly anisotropic shapes, such as rods and wires, can be obtained. In semiconductor nanoparticle synthesis, such growth conditions have been achieved using high precursor, or monomer, concentrations in the growth solution. As discussed previously (Section 1.2), particle-size distributions can be “focused” by maintaining relatively high monomer concentrations that prevent the transition from the fast-growth to the slow-growth (Ostwald ripening) regime.¹⁹ Even higher monomer concentrations can be used to effect a transition from thermodynamic to kinetic growth. Access to the regime of very fast, kinetic growth allows control over particle shape. The system is essentially put into “kinetic overdrive,” where dissolution of particles is minimized as the monomer concentration is maintained at levels higher than the solubility of all of the particles in solution. Growth of all particles is, thereby, promoted.¹⁹ Further, in this regime, the rate of particle growth is not limited by diffusion of monomer to the growing crystal surface, but, rather, by how fast atoms can add to that surface. The relative growth rates of different crystal faces, therefore, have a strong influence over the final particle shape.⁶⁴ Specifically, in systems where the underlying crystal lattice structure is anisotropic, for example, the wurtzite structure of CdSe, simply the presence of high monomer concentrations (kinetic growth regime) at and immediately following nucleation can accentuate the differences in relative growth rates between the unique c -axis and the remaining lattice directions, promoting rod growth. The monomer-concentration-dependent transition from slower-growth to fast-growth regimes coincides with a transition from diffusion controlled to reaction-rate-controlled growth and from dot to rod growth. In general, longer rods are achieved with higher initial monomer concentrations, and rod growth is sustained over time by maintaining high monomer concentrations using multiple-injection techniques. At very low monomer concentrations, growth is supported by intra- and interparticle exchange, rather than by monomer addition from the bulk solution (see discussion later).¹⁷ Finally, these relative rates can be further controlled by judicious choice of organic ligands.^{17,22}

To more precisely tune the growth rates controlling CdSe rod formation, high monomer concentrations are used in conjunction with appropriate organic ligand mixtures. In this way, a wide range of rod aspect ratios has been produced ([Figure 1.16](#)).^{17,22,64} Specifically, the “traditional” TOPO ligand is supplemented with alkyl phosphonic acids. The phosphonic acids are strong metal (Cd) binders and may influence rod growth by changing the relative growth rates of different crystal faces.¹³⁸ CdSe rods form by enhanced growth along the crystallographically unique c -axis (taking advantage of the anisotropic wurtzite crystal structure). Interestingly, the fast growth has

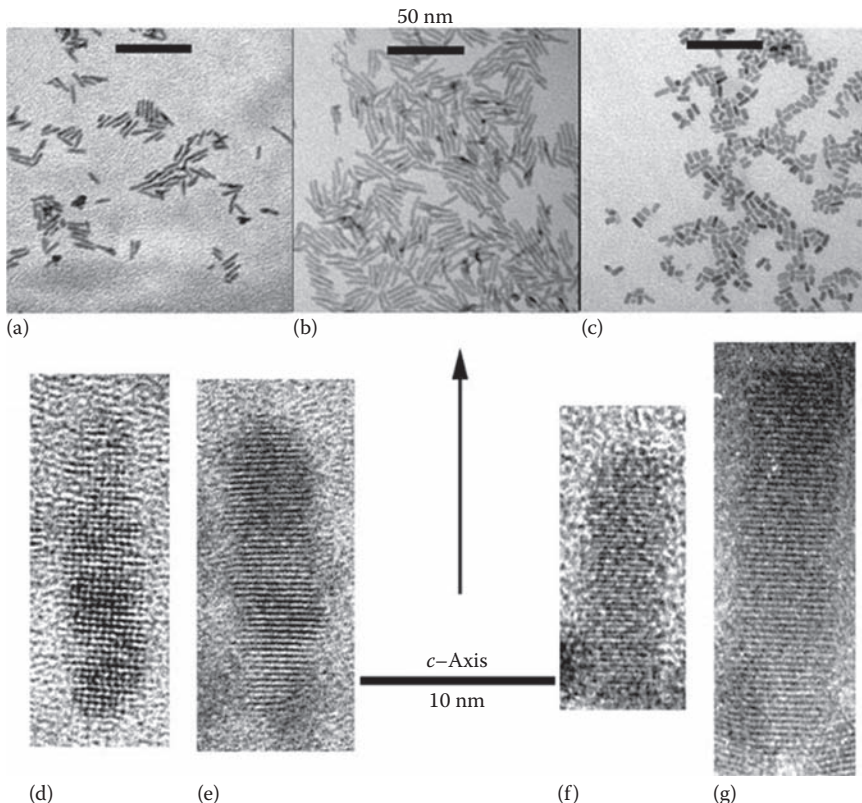


FIGURE 1.16 (a–c) TEMs of CdSe quantum rods demonstrating a variety of sizes and aspect ratios. (d–g) HR-TEMs of CdSe quantum rods revealing lattice fringes and rod growth direction with respect to the crystallographic *c*-axis. (Reprinted with permission from Peng, X., L. Manna, W. Yang, J. Wickham, E. Scher, A. Kadavanich, and A.P. Alivisatos, *Nature*, 404, 59, 2000.)

been shown to be unidirectional—exclusively on the (001) face.⁶⁴ The (001) facets comprise alternating Se and Cd layers, where the Cd atoms are relatively unsaturated (three dangling bonds per atom). In contrast, the related (001) facet exposes relatively saturated Cd faces having one dangling bond per atom (Figure 1.17). Thus, relative to (001), the (001) face (opposite *c*-axis growth) and {110} faces (*ab* growth), for example, are slow growing, and *unidirectional* rod growth is promoted. The exact mechanism by which the phosphonic acids alter the relative growth rates is not certain. Their influence may be in inhibiting the growth of (001) and {110} faces or it may be in directly promoting growth of the (001) face by way of interactions with surface metal sites.⁶⁴ Alternatively, it has been proposed that a more important contribution to the formation of rod-shaped particles by the strong metal ligands is their influence on “monomer” concentrations, where monomer again refers to various molecular precursor species. Specifically, the phosphonic acids may simply *permit* the high monomer

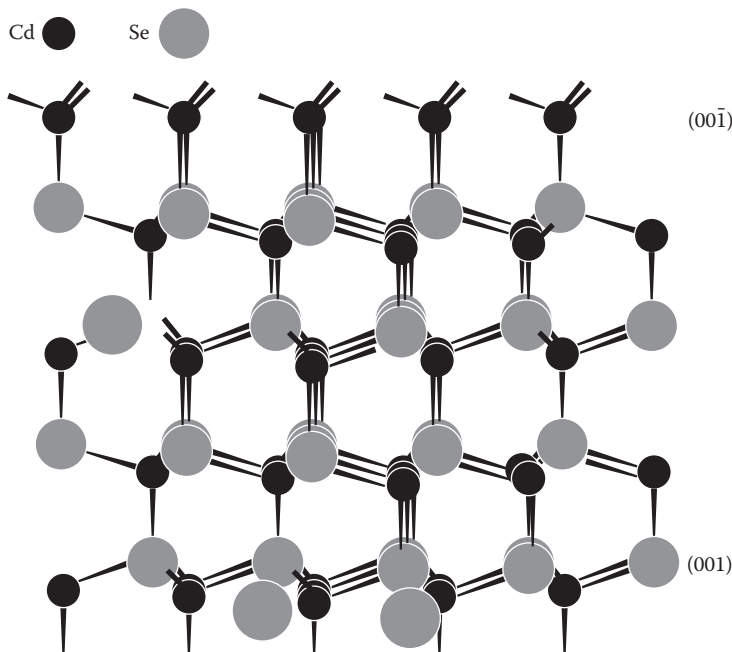


FIGURE 1.17 Atomic model of the CdSe wurtzite crystal structure. The (001) and the (001) crystal faces are emphasized to highlight the different number of dangling bonds associated with each Cd atom (three and one, respectively). (Reprinted with permission from Manna, L., E. C. Scher, and A.P. Alivisatos, *J. Am. Chem. Soc.*, 122, 12700, 2000.)

concentrations that are required for kinetic, anisotropic growth. As strong metal binders, they may coordinate Cd monomers, stabilizing them against decomposition to metallic Cd.¹⁷

More complex shapes, such as “arrows,” “pine trees,” and “teardrops,” have also been prepared in the CdSe system, and the methods used are an extension of those applied to the preparation of CdSe rods. Once again, CdSe appears to be the “proving ground” for semiconductor nanoparticle synthesis. Several factors influencing growth of complex shapes have been investigated, including the time evolution of shape and the ratio of TOPO to phosphonic acid ligands,⁶⁴ as well as the steric bulk of the phosphonic acid.¹⁷ Predictably, reaction temperature also influences the character of the growth regime.^{17,64} In the regime of rod growth, that is., fast kinetic growth, complex shapes can evolve over time. Rods and “pencils” transform into “arrows” and “pine-tree-shaped” particles (Figure 1.18). The sides of the arrow or tree points comprise wurtzite (101) faces. As predicted by traditional crystal growth theory, these slower growing faces have replaced the faster growing (001) face, permitting the evolution to more complex structures.⁶⁴ Shape and shape evolution dynamics were also observed to be highly dependent on phosphonic acid concentrations. Low concentrations (<10 mole%) of hexylphosphonic acid (HPA), for example, relative to TOPO produced approximately spherical particles, while moderate amounts (20 mole%) yielded rods,

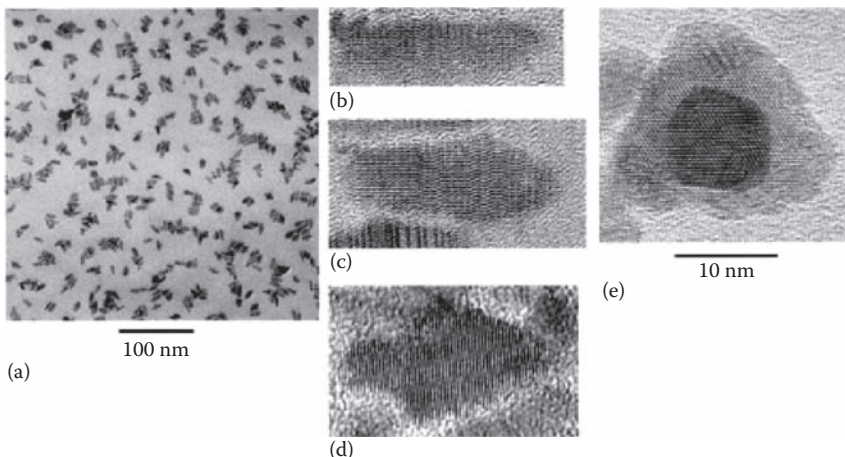


FIGURE 1.18 (a) TEMs of a CdSe NQD sample dominated by arrow-shaped particles (60% HPA reaction). (b–d) HR-TEMs demonstrating the shape evolution from (b) pencil to (c) arrow to (d) pine-tree-shaped CdSe NQDs. (e) Pine-tree-shaped particle looking down the [001] direction, that is, the long axis. Analysis of lattice spacings obtained by HR-TEM imaging revealed that wurtzite is the dominate phase for each shape and that the angled facets of the arrows comprise the (101) faces. (Reprinted with permission from Manna, L., E. C. Scher, and A.P. Alivisatos, *J. Am. Chem. Soc.*, 122, 12700, 2000.)

and high concentrations (60 mole%) resulted in arrow-shaped particles. As discussed previously, HPA appears to enhance the growth of the (001) face *relative* to other crystallographic faces, and higher concentrations simply permit even higher relative growth rates. Therefore, shape evolution to the arrow and tree morphologies proceeds more quickly in the presence of high HPA concentrations. The growth of single-headed arrows, as opposed to double-headed, results from the characteristic unidirectional growth, that is, growth from the (001) face only, and not from the (001) face.

“Teardrop-shaped” particles also arise from the tendency toward unidirectional growth. In this case, rod-shaped crystals are exposed to growth conditions favoring spherical particle shapes—equilibrium slow growth and low-monomer concentrations—causing the rods to become rounded. Monomer concentration is then quickly increased to force elongation of the “droplet” from one end into particles resembling tadpoles.⁶⁴ The growth regime governing the evolution of rods to spherical particles has been termed “1D to 2D intraparticle ripening.”¹⁷ Nanoparticle volumes and total numbers remain approximately constant (as do monomer concentrations), while nanoparticle shape changes dramatically. Intraparticle diffusion of *c*-axis atoms to other crystal faces may explain this transformation. The process is distinguished from “interparticle ripening,” or Ostwald ripening, that is observed at even lower monomer concentrations. Intraparticle ripening is thought to occur when a “diffusion equilibrium” exists between the nanoparticles and the monomers in the bulk solution.¹⁷ Alternatively, it has also been shown that nanodots can be used to “seed” the growth of nanorods. Here, the spherical particles are exposed

to high monomer concentrations that promote one-dimensional (1-D) growth from the template particles. Improved short-axis and aspect-ratio distributions have been reported for these rods ([Figure 1.19](#)).¹⁷

Rod growth dynamics also depend on the identity of the phosphonic acid. The effectiveness of the phosphonic acid in promoting rod growth depends critically on its steric bulk, or the length of its alkyl chain. Shorter-chain phosphonic acids, such as HPA, more effectively promote rod growth compared to longer-chain phosphonic acids, such as tetradecylphosphonic acid (TDPA). Combinations of longer- and shorter-chain phosphonic acids can be used to readily tune rod aspect ratios¹⁷ and control shape evolution dynamics.

The preceding morphologies reflect the underlying wurtzite crystal structure of CdSe. Occasionally, however, CdSe nucleates in the zinc blende phase. When this occurs, a different type of morphology, the tetrapod, is observed. Here, the zinc blende nuclei expose four equivalent (111) faces that comprise the crystallographic equivalent of the wurtzite (001) faces (alternating planes of Cd or Se). From these (111) surfaces, four wurtzite arms' grow unidirectionally. Further addition of monomer either lengthens the wurtzite arms, in the case of purely wurtzite arms, or generates dendritic-like wurtzite branches, when zinc-blende stacking faults are present in the arm ends ([Figure 1.20](#)).⁶⁴

CdSe rod QYs in PL are typically relatively low, ca. 1%–4%. Like their spherical counterparts, however, rods can be overcoated with a higher band-gap inorganic semiconductor, increasing QYs to 14%–20%.^{65,66} Lattice mismatch requirements for rods are somewhat more severe than for spherical particles, and synthetic steps unique to rod overcoating have been employed in the most successful preparations.⁶⁶ As discussed previously (Section 1.3), spherical nanoparticle systems benefit from having highly curved surfaces, compared to less-strain-tolerant planar systems. Nanorods provide an intermediate case. The average curvature of rods lies between that of dots and films, and, due to their larger size/surface area compared to dots, more interfacial strain can accumulate leading to the formation of dislocations. The 12% lattice mismatch between ZnS and CdSe is, therefore, less well tolerated in rods. CdS can be used as a lattice-mismatch “buffer layer” between CdSe and ZnS (only ~4% lattice mismatch with CdSe and ~8% with ZnS). Addition of a small amount of Cd precursor to the shell precursor solution (Cd:Zn of 0.12:1.0) appears to lead to the preferential formation of CdS at the surface of the rods. ZnS growth then proceeds on the CdS. HR TEM images demonstrate uniform and epitaxial growth. Interestingly, QYs remain low, and the benefits of inorganic overcoating in the graded epitaxial approach are only fully realized following photochemical annealing (via laser irradiation) of the rod particles ([Figure 1.21](#)).⁶⁶

1.4.2 SHAPE CONTROL BEYOND CdSe

Solution-phase preparations of unusually shaped and highly anisotropic particles that are soluble, relatively monodisperse, and sufficiently small to exhibit quantum-confinement effects were originally more limited to the CdSe system. Nevertheless, for some time now, CdS and CdTe rod preparations using phosphonic-acid-controlled reactions have been known. In addition, CdS rods and multipods had been prepared in a monosurfactant system in which HDA served both as the stabilizing

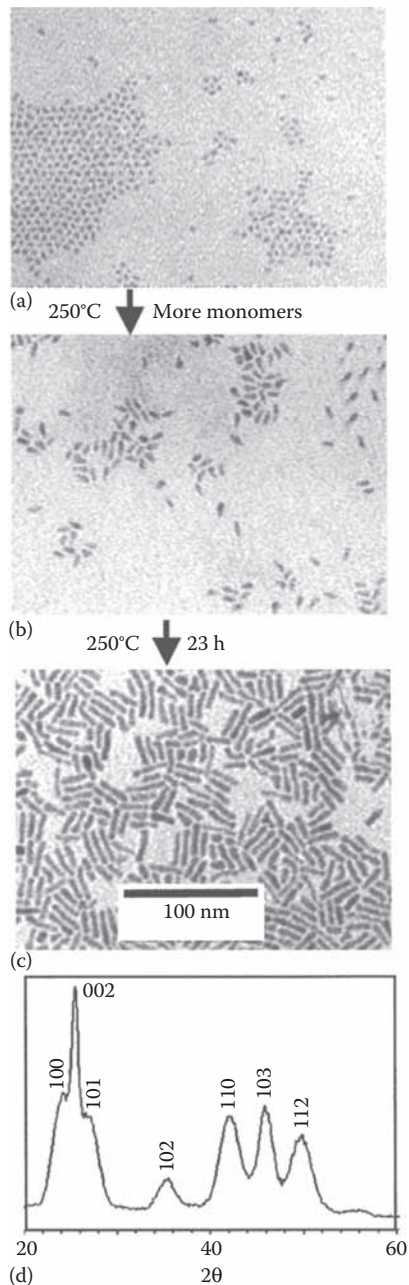


FIGURE 1.19 Seeding CdSe NQD rod growth for improved size monodispersity. (a) TEM of CdSe dots prepared in 13% TDPA using an injection temperature of 360°C and a growth temperature of 250°C. (b) TEM of NQD rods grown from the dot seeds following injection of additional monomer (c) TEM of NQD rods after 23 h of growth. (d) XRD pattern for CdSe rods from (c). (Reprinted with permission from Peng, Z. A. and X. Peng, *J. Am. Chem Soc.*, 123, 1389, 2001.)

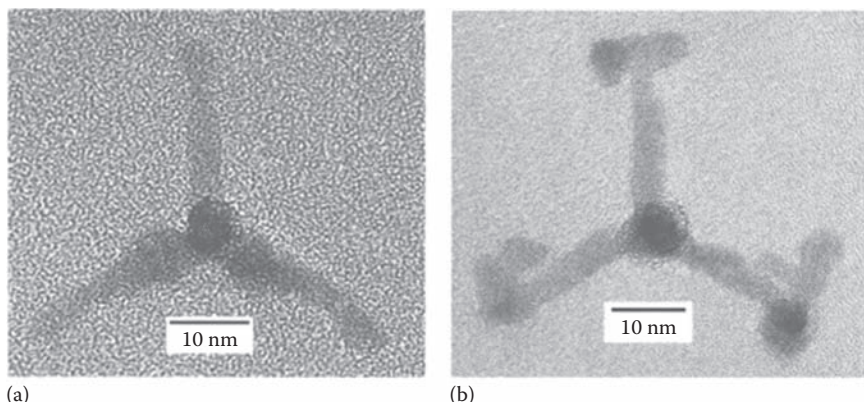


FIGURE 1.20 HR-TEMs of CdSe tetrapods. (a) Image down the [001] direction of one of the four arms. All arms are wurtzite phase, as confirmed by analysis of lattice spacings. (b) “Dendritic” tetrapod, where branches have grown from each arm. Some stacking faults are present in the branches, and zinc-blende layers are present at the ends of the original four arms. (Reprinted with permission from Manna, L., E. C. Scher, and A.P. Alivisatos, *J. Am. Chem. Soc.*, 122, 12700, 2000.)

ligand and the shape-determining ligand.^{67]} Here, rod and multipod formation was temperature dependent. Rods formed at high temperatures ($\sim 300^\circ\text{C}$), while bipods, tripods, and tetrapods dominated at lower temperatures (120°C – 180°C). The dependence of shape on temperature likely resulted from preferential formation of wurtzite CdS nuclei (thermodynamic phase) at high temperatures and zinc blende nuclei (kinetic phase) at lower temperatures. As in the CdSe system, the zinc blende {111} faces can support fast growth of (001) wurtzite “arms.” Significantly, this method allowed isolation of tetrapods in $\sim 82\%$ yield (compared to 15%–40% by the HPA method) at 120°C , though with less control over size (relatively large) compared to their HPA-derived counterparts. Nevertheless, it was the first significant report of solution-based growth of bipod and tripod morphologies in the II-VI system and provided a more predictable method of producing tetrapods.⁶⁷

The same monosurfactant system can be applied to shape-controlled preparation of the magnetic semiconductor, MnS.⁶⁸ At low solution-growth temperatures (120°C – 200°C), MnS prepared from the single-source precursor, $\text{Mn}(\text{S}_2\text{CNEt}_2)_2$, can nucleate in either the zincblende or the wurtzite phase, whereas at high temperatures ($>200^\circ\text{C}$) MnS nucleates in the rock-salt phase. Low-temperature growth yields a variety of morphologies: highly anisotropic nanowires, bipods, tripods and tetrapods (120°C), nanorods (150°C), and spherical particles (180°C). The “single pods” comprise wurtzite cores with wurtzite-phase arms. In contrast, the multipods comprise zinc-blende cores with wurtzite arms, where the arms grow in the [001] direction from the zinc-blende {111} faces, as discussed previously with respect to the Cd-chalcogenide system. Dominance of the isotropic spherical particle shape in reactions conducted at moderate temperatures (180°C) implies a shift from predominantly kinetic control to predominantly thermodynamic control over the temperature

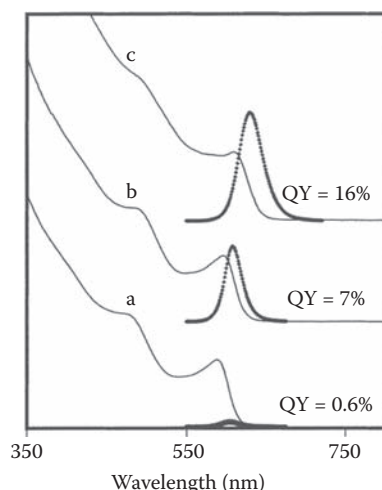


FIGURE 1.21 Absorption (solid line) and PL (dashed line) spectra for medium-length (3.3×21 nm) CdSe nanorods. (a) Core nanorods without ZnS shell. (b) (Core)shell nanorods with thin CdS-ZnS shells (~2 monolayers of shell material, where the CdS “buffer” shell comprises ~35% of the total shell). (c) (Core)shell nanorods with medium CdS-ZnS shells (~4.5 monolayers of shell material, where the CdS “buffer” shell comprises ~22% of the total shell). PL spectra were recorded following photoannealing of the samples. (Reprinted with permission from Manna, L., E. C. Scher, L. S. Li, and A.P. Alivisatos, *J. Am. Chem Soc.*, 124, 7136, 2002.)

range from 120°C to 180°C .⁶⁸ Formation of 1-D particles at low temperatures results from kinetic control of relative growth rates. At higher temperatures, differences in activation barriers to growth of different crystal faces are more easily surmounted, equalizing relative growth rates. Finally, high-temperature growth supports only the thermodynamic rock-salt structure, large cubic crystals. Also, by combining increased growth times with low growth temperatures, shape evolution to higher-temperature shapes is achieved.⁶⁸

Extension of the ligand-controlled shape methodology to highly symmetric cubic crystalline systems is also possible. Specifically, PbS, having the rock-salt structure, can be prepared as rods, tadpole-shaped monopods, multipods (bipods, tripods, tetrapods, and pentapods), stars, truncated octahedra, and cubes.⁶⁹ The rod-based particles, including the mono- and multipods, retain short-axis dimensions that are less than the PbS Bohr exciton radius (16 nm) and, thus, can potentially exhibit quantum-size effects. These highly anisotropic particle shapes represent truly metastable morphologies for the inherently isotropic PbS system. The underlying PbS crystal lattice is the symmetric rock-salt structure, the thermodynamically stable manifestations of which are the truncated octahedra and the cubic nanocrystals. The PbS particles are prepared by pyrolysis of a single source precursor, $\text{Pb}(\text{S}_2\text{CNEt}_2)_2$, in hot phenyl ether in the presence of a large excess of either a long-chain alkyl thiol or amine. The identity of the coordinating ligand and the solvent temperature determine the initial particle shape following injection (Figure 1.22). Given adequate time,

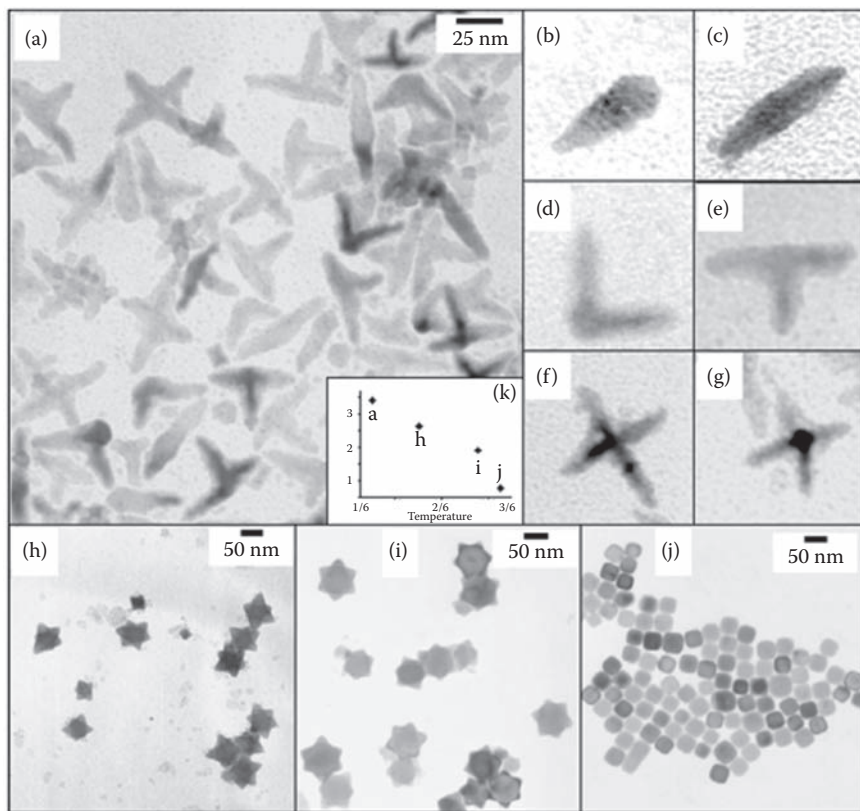


FIGURE 1.22 TEMs showing the variety of shapes obtained from the PbS system grown from the single-source precursor, $\text{Pb}(\text{S}_2\text{CNEt}_2)_2$, at several temperatures. (a) Multipods prepared at 140°C. (b) Tadpole-shaped monopod (140°C). (c) I-shaped bipod (140°C). (d) L-shaped bipod (140°C). (e) T-shaped tripod (140°C). (f) Cross-shaped tetrapod (140°C). (g) Pentapod (140°C). (h) Star-shaped nanocrystals prepared at 180°C. (i) Rounded star-shaped nanocrystals prepared at 230°C. (j) Truncated octahedra prepared at 250°C. (Reprinted with permission from Lee, S. M., Y. Jun, S. N. Cho, and J. Cheon, *J. Am. Chem Soc.*, 124, 11244, 2002.)

particle shapes evolve from the metastable rods to the stable truncated octahedron and cubes, with star-shaped particles comprising energetically intermediate shapes.⁶⁹

As in the CdSe system, the particle shape in the cubic PbS system depends intimately on the ligand concentration and its identity. The highest ligand concentrations yield a reduced rate of growth from the {111} faces compared to the {100} faces, which experience enhanced relative growth rates. Further, alkylthiols are more effective at controlling relative growth rates compared to alkylamines. The latter, a weaker Pb binder, consistently leads to large, thermodynamically stable cubic shapes. Finally, reaction temperature plays a key role in determining particle morphology. The lowest temperatures (140°C) yield the metastable rod-based morphologies, with intermediate star shapes generated at moderate temperatures (180°C–230°C) and truncated octahedra

isolated at the highest temperatures (250°C). Interestingly, the rod structures appear to form by preferential growth of {100} faces from truncated octahedra seed particles. For example, the “tadpole” shaped monopods are shown by HRTEM studies to comprise truncated octahedra “heads” and [100]-axis “tails,” resulting from growth from a (100) face. The star-shaped particles that form at 180°C are characterized by six triangular corners, comprising each of the six {100} faces. The {100} faces have shrunk into these six corners as a result of their rapid growth, similar to the replacement of the (001) face by slower growing faces during the formation of arrow-shaped CdSe particles (see preceding text). The isolation of star-shaped particles at intermediate temperatures suggests that the relative growth rates of the {100} faces remain enhanced compared to the {111} faces at these temperatures. Further, the overall growth rate is enhanced as a result of the higher temperatures. The star-shaped particles that form at 230°C are rounded and represent a decrease in the differences in relative growth rates between the {100} faces and the {111} faces, the latter, higher-activation-barrier surface benefiting from the increase in temperature. A definitive shift from kinetic growth to thermodynamic growth is observed at 250°C (or at long growth times). Here, the differences in reactivity between the {100} and the {111} faces are negligible given the high thermal energy input that surmounts either face’s activation barrier. The thermodynamic cube shape is, therefore, approximated by the shapes obtained under these growth conditions. In all temperature studies, the alkylthiol:precursor ratio was ~80:1, and monomer concentrations were kept high—conditions supporting controlled and kinetic growth, respectively.

1.4.3 FOCUS ON HETEROSTRUCTURED ROD AND TETRAPOD MORPHOLOGIES

Recently, vast progress has been made in terms of controlled growth of anisotropic nanostructures, especially tetrapods,⁷⁰ and particular attention has been given to extending synthesis procedures to *heterostructured* rods^{71–76} and tetrapods.^{74,77,78} Compositional heterostructuring in anisotropic systems (e.g., CdTe/CdSe rods and tetrapods) provides for the possibility of establishing “built-in” electric fields for forcing the depletion or accumulation of electrons and holes within the particle. Such control over charge carriers is advantageous for optoelectronic applications, such as photovoltaics, light-emitting diodes, and sensors.⁷⁶ Furthermore, heterostructuring can facilitate the formation of electrical contacts with nanoscale structures, as in the case of “gold-tipped” rods and tetrapods.⁷¹ Importantly, unlike (core)shell concentric heterostructured systems, for which heterostructuring can be limited by lattice-mismatch-induced strain effects, rod/tetrapod-based heterostructured systems are perhaps more “fully tunable,” as they do not suffer from this constraint.⁷⁷ Finally, it is worth noting that preferential growth of specific geometries remains a synthetic challenge. Several “seeding” approaches have been described that attempt to address this issue. By seeding growth with either wurtzite or zinc-blende CdSe nanocrystals, CdSe/CdS heterostructured rods and tetrapods can be selectively formed, respectively, for which “giant” extinction coefficients and high QYs in emission (~80 and ~50%, respectively)—by way of energy transfer from the CdS regions to the emitting CdSe core—are obtained.⁷⁴ Alternatively, noble-metal nanoparticles have been used as seeds for inducing rod and “multipod” growth, where the specific shape of the nanocrystal (in this case CdSe) depends on the choice of the metallic seeds (Au, Ag, Pd, or Pt) and the reaction time.⁷⁹

1.4.4 SOLUTION–LIQUID–SOLID NANOWIRE SYNTHESIS

III-V semiconductors have proven amenable to solution-phase control of particle shape using an unusual synthetic route. Specifically, the method involves the solution-based catalyzed growth of III-V nanowiskers.⁸⁰ In this method, referred to as the “solution–liquid–solid mechanism,” a dispersion of nanometer-sized indium droplets in an organometallic reaction mixture serves as the catalytic sites for precursor decomposition and nanowhisker growth. As initially described, the method afforded no control over nanowhisker diameters, producing very broad diameter distributions and mean diameters far in excess of the strong-confinement regime for III-V semiconductors. Additionally, the nanowhiskers were insoluble, aggregating, and precipitating upon growth. However, recent studies have demonstrated that the nanowhiskers mean diameters and diameter distributions are controlled through the use of near-monodisperse metallic-catalyst nanoparticles.^{81,82} The metallic nanoparticles are prepared over a range of sizes by heterogeneous seeded growth.⁸³ The solution–liquid–solid mechanism in conjunction with the use of these near-monodisperse catalyst nanoparticles and polymer stabilizers affords soluble InP and GaAs nanowires having diameters in the range of 3.5–20 nm and diameter distributions of $\pm 15\%$ –20% (Figure 1.19). The absorption spectra of the InP quantum wires contain discernible excitonic features from which the size dependence of the band gap has been determined, and quantitatively compared to that in InP QDs.⁸² II-VI quantum wires can also be grown in a similar manner.⁸⁴ A similar approach was applied to the growth of insoluble, but size-monodispersed in diameter (4–5 nm), silicon nanowires. Here, reactions were conducted at elevated temperature and pressure (500°C and 200–270 bar) using alkanethiol-coated gold nanoclusters (2.5 ± 0.5 nm diameter) as the nucleation and growth “seeds.”⁸⁵ Recently, substantial progress has been made in the solution–liquid–solid growth of III-V, II-VI, and IV-VI semiconductor nanowires,^{86,87} including initial success with respect to axial^{88,89} and radial heterostructuring,⁸⁸ as well as the formation of branched homo- and heterostructures.⁹⁰

1.5 PHASE TRANSITIONS AND PHASE CONTROL

1.5.1 NQDs UNDER PRESSURE

NQDs have been used as model systems to study solid–solid phase transitions.^{91,91–94} The transitions, studied in CdSe, CdS, InP, and Si nanocrystals,⁹³ were induced by pressure applied to the nanoparticles in a diamond anvil cell by way of a pressure-transmitting solvent medium, ethyl-cyclohexane. Such transitions in bulk solids are typically complex and dominated by

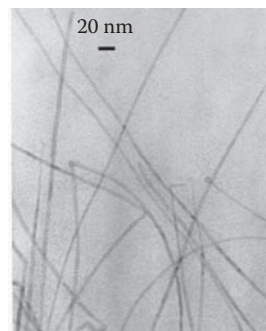


FIGURE 1.23 TEM of InP quantum wires of diameter 4.49 ± 0.75 ($\pm 17\%$), grown from 9.88 ± 0.795 ($\pm 8.0\%$) In-catalyst nanoparticles. The values following the “ \pm ” symbols represent one standard deviation in the corresponding diameter distribution. (Reprinted with permission from Yu, H., J. Li, R. A. Loomis, L.-W. Wang, and W. E. Buhro, *Nat. Mater.*, 2, 517, 2003.)

multiple nucleation events, the kinetics of which are controlled by crystalline defects that lower the barrier height to nucleation.^{91,94} In nearly defect-free nanoparticles, the transitions can exhibit single-structural-domain behavior and are characterized by large kinetic barriers (Figure 1.24). In contrast to original interpretations, which described the phase transition in nanocrystals as “coherent” over the entire nanocrystal,⁹¹ the nucleation of the phase transition process was recently shown to be localized to specific crystallographic planes.⁹⁴ The simple unimolecular kinetics of the transition still support a single nucleation process; however, the transition is now thought to result from plane sliding as opposed to a coherent deformation process. Specifically, the sliding plane mechanism involves shearing motion along the (001) crystallographic planes, as supported by detailed analyses of transformation times as a function of pressure and temperature.

Because of the large kinetic barriers in nanocrystal systems, their phase transformations are characterized by hysteresis loops (Figure 1.24).^{91,92,94} The presence of a strong hysteresis signifies that the phase transition does not occur at the thermodynamic transition pressure and that time is required for the system to reach an equilibrium state. This delay is fortunate in that it permits detailed analysis of the transition kinetics even though the system is characterized by single-domain (finite-size) behavior. As alluded to, these analyses were used to determine the structural mechanism for transformation. Specifically, kinetics studies of transformation times as a function of temperature and pressure were used to determine relaxation times, or average times to overcome the kinetic barrier, and, thereby, rate constants. The temperature dependence of the rate

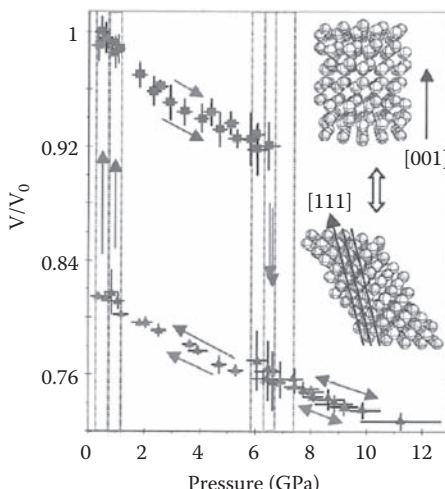


FIGURE 1.24 Two complete hysteresis cycles for 4.5 nm CdSe NQDs presented as unit cell volumes for the wurtzite sixfold-coordinated phase (triangles) and the rock-salt fourfold-coordinated phase (squares) versus pressure. Solid arrows indicate the direction of pressure change, and dotted boxes indicate the mixed-phase regions. Unlike bulk phase transitions, the wurtzite to rock-salt transformation in nanocrystals is reversible and occurs without the formation of new high-energy defects, as indicated by overlapping hysteresis loops. The shape change that a sliding-plane transformation mechanism (see text) would induce is shown schematically on the right. (Reprinted with permission from Wickham, J. N., A. B. Herhold, and A.P. Alivisatos, *Phys. Rev. Lett.*, 84, 923, 2000.)

constants led to the determination of activation energies for the forward and reverse transitions, and the pressure dependence of the rate constants led to the determination of activation volumes for the process.⁹⁴ The latter represents the volume change between the starting structure and an intermediate transitional structure. Activation volumes for the two directions, wurtzite to rock salt and rock salt to wurtzite, respectively, were unequal and smaller for the latter, implying that the intermediate structure more closely resembles the 4-coordinate structure. The activation volumes were also shown to be of opposite sign, indicating that the mechanism by which the phase transformation takes place involves a structure whose volume is in between that of the two end phases. Most significantly, the magnitude of the activation volume is small compared to the total volume change that is characteristic of the system (~0.2% versus 18%). The activation volume is equal to the critical nucleus size responsible for initiating the phase transformation—*defining the volume change associated with the nucleation event.*

The small size of the activation volume suggests that the structural mechanism for transformation cannot be a coherent one involving the entire nanocrystal.⁹⁴ Spread out over the entire volume of the nanocrystal, the activation volume would amount to a volume change smaller than that induced by thermal vibrations in the lattice. Therefore, a mechanism involving some fraction of a nanocrystal was considered. The nucleus was determined not to be three-dimensional (3-D); as a sphere the size of the activation volume would be less than a single-unit cell. Also, activation volumes were observed to increase with increasing particle size (in the direction of increasing pressure). There is no obvious mechanistic reason for a spherically shaped nucleus to increase in size with an increase in particle size. Further, additional observations have been made: (1) particle shape changes from cylindrical or elliptical to slab-like upon transformation from the 4-coordinate to the 6-coordinate phase,⁹² (2) the stacking-fault density increases following a full pressure cycle from the 4-coordinate through the 6-coordinate and back to the 4-coordinate structure,⁹² and (3) the entropic contribution to the free-energy barrier to transformation increases with increasing size (indicating that the nucleation event can initiate from multiple sites).⁹⁴ Together, the various experimental observations suggest that the mechanism involves a directionally dependent nucleation process that is not coherent over the whole nanocrystal. The specific proposed mechanism entails shearing of the (001) planes, with precedent found in martensitic phase transitions ([Figure 1.25](#))^{92,94} Further, the early observation that activation energy increases with size⁹¹ likely results from the increased number of chemical bonds that must be broken for plane sliding to occur in large nanocrystals, compared to that in small nanocrystals. Such a mechanistic-level understanding of the phase transformation processes in nanocrystals is important as nanocrystal-based studies, due to their simple kinetics, may ultimately inform a better understanding of the hard-to-study, complex transformations that occur in bulk materials and geologic solids.⁹⁴

1.5.2 NQD GROWTH CONDITIONS YIELD ACCESS TO NONTHERMODYNAMIC PHASES

Phase control, much like shape control (Section 1.4), can be achieved in nanocrystal systems by operating in kinetic growth regimes. Materials synthesis strategies have typically relied upon the use of reaction conditions far from standard temperature

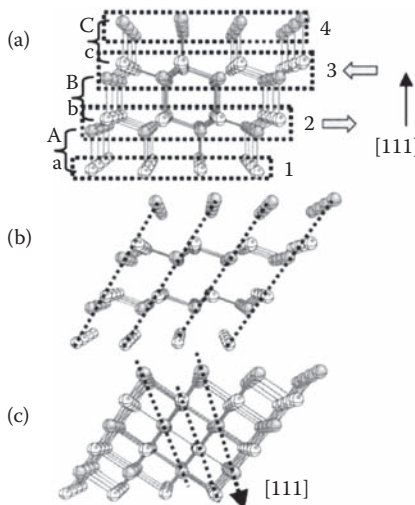


FIGURE 1.25 Schematic illustrating the sliding-plane transformation mechanism. (a) Zinc-blende structure, where brackets denote (111) planes, dashed boxes show planes that slide together, and arrows indicate the directions of movement. (b) Structure of (a) after successive sliding has occurred. (c) Rock-salt structure, where dashed lines denote (111) planes. Structures are oriented the same in (a–c). (Reprinted with permission from Wickham, J. N., A. B. Herhold, and A.P. Alivisatos, *Phys. Rev. Lett.*, 84, 923, 2000.)

and pressure (STP) to obtain nonmolecular materials such as ceramics and semiconductors. The crystal-growth barriers to covalent nonmolecular solids are high and have historically been surmounted by employing relatively extreme conditions, comprising a direct assault on the thermodynamic barriers to solid-state growth. The interfacial processes of adsorption–desorption and surface migration permit atoms initially located at nonlattice sites on the surface of a growing crystal to relocate to a regular crystal lattice position. When these processes are inefficient or not functioning, amorphous material can result. Commonly, synthesis temperatures of $\geq 400^{\circ}\text{C}$ are required to promote these processes leading to crystalline growth.^{95,96} Such conditions can preclude the formation of kinetic, or higher-energy, materials and can limit the selection of accessible materials to those formed under thermodynamic control—the lowest-energy structures.^{97,98} In contrast, biological and organic–chemical synthetic strategies, often relying on catalyzed growth to surmount or lower-energy barriers, permit access to both lowest-energy and higher-energy products,⁹⁷ as well as access to a greater variety of structural isomers compared to traditional, solid-state synthetic methods. The relatively low-temperature, surfactant-supported, solution-based reactions employed in the synthesis of NQDs provide for the possibility of forming kinetic phases, that is, those phases that form the fastest under conditions that prevent equilibrium to the lowest-energy structures. Formation of the CdSe zinc-blende phase, as opposed to the wurzite structure, is likely a kinetic product of low-temperature growth. In general, however, examples are relatively limited. More examples are to be found in the preparation of nonmolecular *solid*

thin films: electrodeposition onto single-crystal templating substrates,⁹⁹ chemical vapor deposition using single-source precursors having both the target elements and the target structure built-in,¹⁰⁰ and reaction of nanothin film, multilayer reactants to grow metastable, SL compounds.^{101–103} One clear example from the solution phase is that of the formation of the metastable, previously unknown, rhombohedral InS (R-InS) phase.¹⁰⁴ The organometallic precursor, *t*-Bu₃In was reacted with H₂S(g) at ~200°C in the presence of a protic reagent, benzenethiol. This reagent provided the apparent dual function of catalyzing efficient alkyl elimination and supplying some degree of surfactant stabilization. Although the starting materials were soluble, the final product was not. Nevertheless, characterization by TEM and powder x-ray diffraction (XRD) revealed that the solid-phase product was a new layered InS phase, structurally distinct from the thermodynamic network structure, orthorhombic β-InS. Further, the new phase was 10.6% less dense compared to β-InS, and was, therefore, predicted to be a low-T, kinetic structure. To confirm the relative kinetic–thermodynamic relationship between R-InS and β-InS, the new phase was placed back into an organic solvent (reflux T ~200°C) in the presence of a molten indium metal flux. The metal flux (molten nanodroplets) provided a convenient recrystallization medium, effecting *equilibration* of the layered and network structures allowing conversion to the more stable, thermodynamic network β-InS. The same phase transition can occur by simple solid-state annealing; however, significantly higher temperatures (>400°C) are required. That the flux-mediated process involves true, direct conversion of one phase to the other (rather than dissolution into the flux followed by nucleation and crystallization) was demonstrated by subjecting a sample powder containing significant amorphous content to the metal flux. The time required for complete phase transformation was several times that of the simple R-InS to β-InS conversion.

1.6 NANOCRYSTAL DOPING

Incorporation of dopant ions into the crystal lattice structure of an NQD by direct substitution of constituent anions or cations involves synthetic challenges unique to the nanosize regime. Doping in nanoparticles entails synthetic constraints not present when considering doping at the macroscale. The requirements for relatively low growth temperatures (for solvent/ligand compatibility and controlled growth) and for low posttreatment temperatures (to prevent sintering), as well as the possible tendency of nanoparticles to efficiently exclude defects from their cores to their surfaces (see Section 1.5) are nanoscale phenomena. Dopant ions in such systems can end up in the external sample matrix, bound to surface ligands, adhered directly to nanoparticle surfaces, doped into near-surface lattice sites, or doped into core lattice sites.¹⁰⁵

Given their dominance in the literature thus far, this section will focus on a class of doped materials known, in the bulk phase, as dilute magnetic semiconductors (DMS). A thorough and current review of NQD doping can be found in Chapter 11, while this section emphasizes the early history of this subfield. Semiconductors, bulk or nanoparticles, that are doped with magnetic ions are characterized by a sp–d exchange interaction between the host and the dopant, respectively. This interaction

provides magnetic and magneto-optical properties that are unique to the doped material. In the case of doped nanoparticles, the presence of a dopant paramagnetic ion can essentially mimic the effects of a large external magnetic field. Magneto-optical experiments are, therefore, made possible merely by doping. For example, fluorescence line narrowing studies on Mn-doped CdSe NQDs are consistent with previous studies on *undoped* NQDs in an external magnetic field.¹⁰⁵ Further, *nano-sized* DMS materials provide the possibility for additional control over material properties as a result of enhanced carrier spatial confinement. Specifically, unusually strong interactions between electron and hole spins and the magnetic ion dopant should exist [106,107]. Such carrier spin interactions were observed in Cd(Mn)S¹⁰⁶ and Zn(Mn)Se¹⁰⁷ as giant splitting of electron and hole spin sublevels using magnetic circular dichroism (MCD). Under ideal dopant conditions—a single Mn ion at the center of an NQD—it is predicted that significantly enhanced spin-level splitting, compared to that in bulk semimagnetic semiconductors, would result.¹⁰⁶ Host–dopant interactions are also apparent in simple PL experiments. Emission from a dopant ion such as Mn²⁺ can occur by way of energy transfer from NQD host to dopant and can be highly efficient (e.g., QY = 22% at 295 K and 75% below 50 K¹⁰⁷) (Figure 1.26). The dopant emission signal occurs to the red of the NQD emission signal, or it overlaps NQD PL if the latter is dominated by deep-trap emission. Its presence has been cited as evidence for successful doping; however, the required electronic coupling can exist even when the “dopant” is located outside of the NQD.¹⁰⁵ Therefore, other methods are now preferred in determining the success or failure of a doping procedure.

Successful “core” doping was first achieved using low-temperature growth methods, such as room-temperature condensation from organometallic precursors in the presence of a coordinating surfactant¹⁰⁸ or room-temperature inverse-micelle methods.^{109–111} Unfortunately, due to relatively poor NQD crystallinity or surface passivation, PL from undoped semiconductor nanoparticles prepared by such methods is generally characterized by weak and broad deep-trap emission. Thus, NQD quality is not optimized in such systems. Other low-temperature methods commonly used to prepare “doped” nanocrystals have been shown to yield only “dopant-associated” nanocrystals. For example, the common condensation reaction involving completely uncontrolled growth performed at room temperature by simple aqueous-based coprecipitation from inorganic salts (e.g., Na₂S and CdSO₄, with MnSO₄ as the dopant source), in the absence of organic ligand stabilizers, yields agglomerates of nano-sized domains and *unincorporated* dopant.¹¹³ Cd and ¹H NMR were used to demonstrate that Mn²⁺ remained outside of the NQD in these systems.¹¹² Doping into the crystalline lattice, therefore, appears to require some degree of control over particle growth when performed *at room temperature* (i.e., excluding higher-temperature, solid-state pyrolysis reactions that can yield well-doped nanocrystalline, though *not* quantum confined [$>20\text{ nm}$], material in the absence of any type of ligand control or influence.¹¹³) The ability to distinguish between surface-associated and truly incorporated dopant ions is critical. For example, both can provide the necessary electronic coupling to achieve energy transfer and the resultant dopant emission signal. Various additional characterization methods have been employed, such as nuclear magnetic resonance (NMR) spectroscopy,^{105,112} electron paramagnetic resonance (EPR),^{68,105–107,109,114}

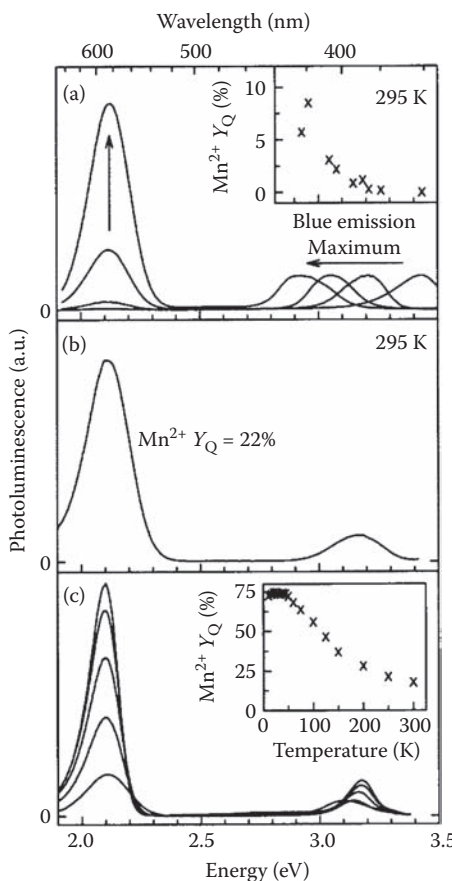


FIGURE 1.26 (a) PL spectra taken at 295 K for a size-series of Mn-doped ZnSe NQDs. As ZnSe emission (“blue emission”) shifts to lower energies with increasing particle size, Mn emission increases in intensity. The particle diameters represented are <2.7, 2.8, 4.0, and 6.3 nm. The reaction Mn concentration (C_1) for each is 2.5%, where the actual (doped) concentration is \sim 1–5% of C_1 . The inset shows Mn emission QY (Y_Q) versus the ZnSe emission maximum. (b) PL spectrum and Mn²⁺ QY (22%) for 2.85 nm Mn-doped ZnSe NQDs prepared using a C_1 of 6.3%. (c) Temperature-dependent PL spectra for doped NQDs from (b); QY reaches a maximum of 75% below 50 K. (Reprinted with permission from Norris, D. J., N. Yao, F. T. Charnock, and T. A. Kennedy, *Nano Lett.*, 1, 3, 2001.)

powder XRD, x-ray absorption fine structure spectroscopy (XAFS),¹¹⁴ chemical treatments (e.g., surface exchange reactions and chemical etching; see later),^{68,105} and ligand-field electronic absorption spectroscopy (see later).¹¹⁵

Recently, doped NQDs have been prepared by high-temperature pyrolysis of organometallic precursors in the presence of highly coordinating ligands: Zn(Mn)

Se at an injection temperature of 310°C ¹⁰⁷ and Cd(Mn)Se at an injection temperature of 350°C .¹⁰⁵ The undoped NQDs prepared by such methods are very well size selected (~4%–7%), highly crystalline, and well passivated.^{105,107} However, the dopant is incorporated into the NQD at low levels ($\sim\!1$ Mn per NQD). Despite input concentrations of ~0.5%–5% dopant precursor, dopant incorporation is only ~0.025%–0.125%. In the Cd(Mn)Se system, for example, Mn^{2+} incorporation into CdSe was limited to near-surface lattice sites, while the remaining Mn^{2+} was present merely as surface-associated ions. The location of the dopant ions following DMS NQD preparation was elucidated using a combination of chemical surface treatments and EPR measurements. Surface exchange reactions, involving thorough replacement of TOPO/TOP capping ligands for pyridine, revealed that much of the dopant cations were only loosely associated with the NQD surface. EPR spectra following surface exchange showed a dramatic decrease in intensity following surface exchange (Figure 1.27), indicating that the majority of dopant ions were not successfully incorporated into the CdSe crystal lattice. Further, even limited incorporation of Mn into the CdSe lattice apparently required the use of a single-source Mn-Se precursor [$\text{Mn}_2(\mu\text{-SeMe})_2(\text{CO})_8$], rather than a simple Mn-only precursor

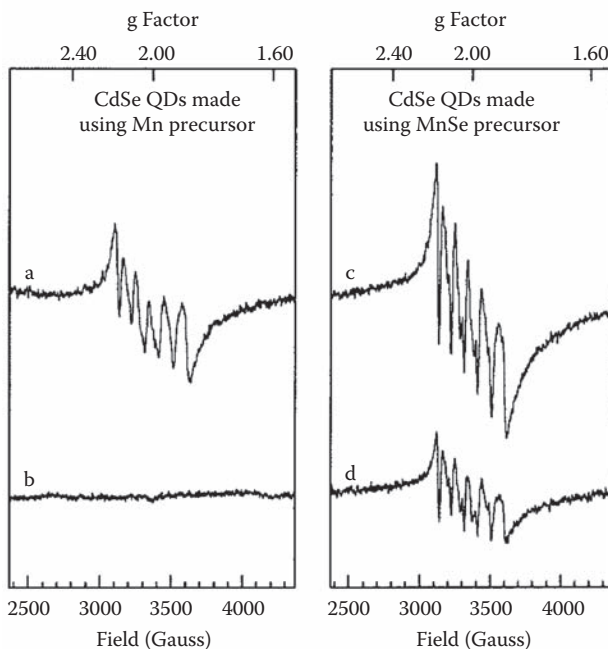


FIGURE 1.27 Low-temperature (5 K) EPR spectra of 4.0 nm diameter Mn-doped CdSe NQDs prepared using (a and b) a Mn-only precursor and (c and d) the $\text{Mn}_2(\mu\text{-SeMe})_2(\text{CO})_8$ single-source precursor. Before purification (a and c), both samples display the 6-line pattern characteristic of Mn. After pyridine cap exchange (b and d), only the sample prepared with the single-source precursor retains the Mn signal. (Reprinted with permission from Mikulec, F. V., M. Kuno, M. Bennati, D. A. Hall, R. G. Griffin, and M. G. Bawendi, *J. Am. Chem. Soc.*, 122, 2532, 2000.)

(e.g., MnMe_2 , $\text{Mn}(\text{CO})_5\text{Me}$, $(\text{MnTe}(\text{CO})_3(\text{PEt}_3)_2)_2$). In the absence of the single-source dopant precursor, which possibly facilitated Mn^{2+} incorporation by supplying pre-formed Mn–Se bonds, EPR spectra following surface exchange with pyridine were structureless ([Figure 1.27a and b](#)). Further, in the case of $\text{Cd}(\text{Mn})\text{Se}$, chemical etching experiments were conducted to remove surface layers of the NQDs and, with them, any dopant that resided in these outer lattice layers. Etching revealed that the distribution of Mn in the CdSe was *not random*. Most Mn^{2+} dopant ions resided in the near-surface layers, and only a small fraction resided near the core. These results are suggestive of a “zone-refining” process¹⁰⁵ and are possibly consistent with the previously discussed notion that NQDs exclude defects. In the case of $\text{Zn}(\text{Mn})\text{S}$ DMSs, EPR and MCD experiments demonstrated that the majority of Mn^{2+} dopant resided well inside the NQD in high-symmetry, cubic Zn lattice sites. The dominant EPR signal comprised 6-line spectra that exhibited hyperfine splitting of $60.4 \times 10^{-4} \text{ cm}^{-1}$, similar to the splitting observed for Mn in bulk ZnSe ($61.7 \times 10^{-4} \text{ cm}^{-1}$).¹⁰⁷ Also, the presence of giant spin sublevel splitting at zero applied field, as demonstrated by MCD, provided additional evidence that the Mn^{2+} dopant resided inside the NQD. The dopant-induced sublevel splitting occurs only when there is wavefunction overlap between the dopant and the confined electron–hole pair, that is, only when Mn^{2+} resides inside the NQD.^{106,107}

Sufficient experimental work has been conducted to begin to make a few general statements regarding solution-based preparation of DMS NQDs and the synthetic parameters that most strongly influence the success of the doping process. First, dopant ions can possibly be excluded from the interior of the NQD to near-surface lattice sites when high-temperature nucleation and growth is employed¹⁰⁵ or limited (apparently) to ~ 1 dopant ion per NQD under such high-temperature conditions.^{105,107} Lower-temperature approaches appear to provide higher doping levels. For example, a moderate-temperature organometallic-precursor approach was recently used to successfully internally dope CdS with Mn at very high levels: 2%–12% as indicated by changes in XRD patterns with increasing Mn concentrations ([Figure 1.28](#)) (EPR hyperfine structure consistent with high-symmetry coordination of the dopant cations was most convincing for dopant concentrations $\leq 4\%$; [Figure 1.29](#)).⁶⁸ Apparent exclusion from the lattice was only observed at dopant levels $> 15\%$. Single-source precursors were used for both core and dopant ions [$\text{Cd}(\text{S}_2\text{CNEt}_2)_2$ and $\text{Mn}(\text{S}_2\text{CNEt}_2)_2$, respectively], and the reaction temperature was 120°C. The particles were rather large and rod-shaped ([Figure 1.30](#)). Significantly, if repeated at 300°C, dopant levels were limited to $< 2\%$ Mn.⁶⁸ Additional temperature effects have been observed in annealing studies. Specifically, in $\text{Cd}_{0.95}\text{Mn}_{0.05}\text{S}$ NQDs, it has been postulated that postpreparative heat treatment can force Mn^{2+} to the surface. The Mn^{2+} PL signal decreases to zero following anneal treatments above 200°C, and no Mn is detected by EDS following anneal treatments above 120°C.¹¹⁶ Finally, low-temperature inverse-micelle reactions appear to benefit from an aging process. The micelle solutions are allowed to age before ligand stabilization and workup. This process is thought to entail particle growth by Ostwald ripening and concurrent loss of dopant leading to 40%–60% less Mn^{2+} ¹¹⁰ or Co^{2+} ¹¹⁵ in CdS particles. The resultant DMS NQDs, however, are of superior quality compared to unaged particles. For example, electronic absorption spectroscopy

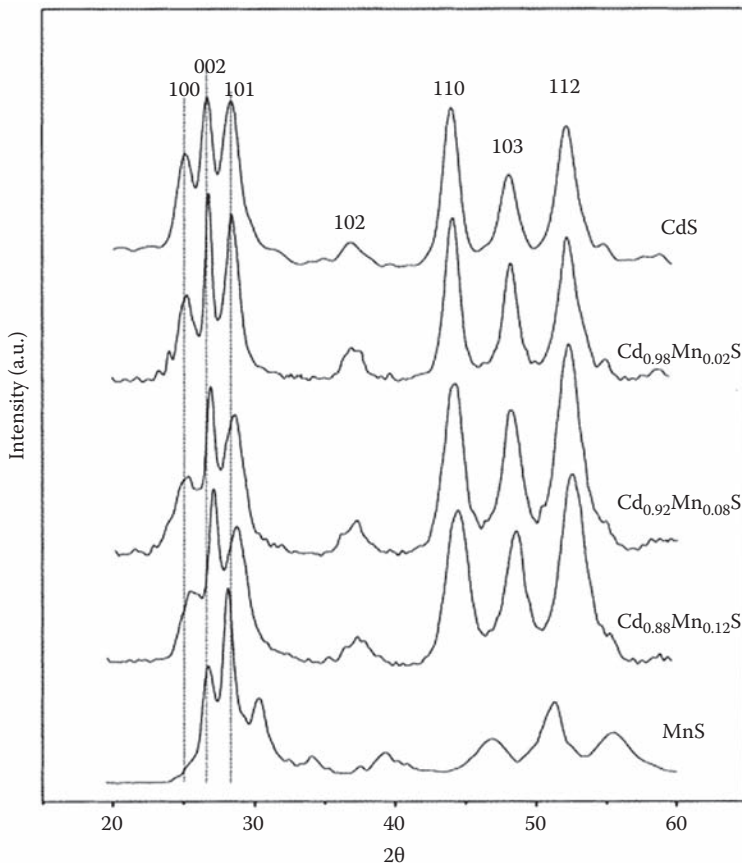


FIGURE 1.28 XRD patterns for $\text{Cd}_{1-x}\text{Mn}_x\text{S}$ nanorods, where x in the doped samples varies from 2 to 8 to 12%. Peaks shift to higher 2θ with increasing Mn concentration. The magnitudes of the observed shifts are consistent with that predicted by Vegard's Law, indicating a homogeneous distribution of Mn within the CdS matrix. (Reprinted with permission from Jun, Y., Y. Jung, and J. Cheon, *J. Am. Chem Soc.*, 124, 615, 2002.)

has been used to demonstrate a change in local environment for Co^{2+} in CdS NQDs dissolved in pyridine (a coordinating solvent) for unaged and aged samples. Unaged samples are dominated by surface-bound Co^{2+} ($\text{Co}(\mu_4\text{-S})_2(\text{N(py)})_2$) and $\text{Co}(\mu_4\text{-S})_3(\text{N(py)})_1$, where $(\mu_4\text{-S})$ refers to “lattice sulfides” and N(py) to pyridine-coordination), whereas entirely lattice-bound Co^{2+} ($\text{Co}(\mu_4\text{-S})_4$) prevails in aged samples.¹¹⁵ Interestingly, the aging process, which requires approximately up to several days, can be substituted by an isocrystalline shell-growth process that requires only minutes to complete. In other words, following particle formation but before ligand stabilization, additional Cd and S (or Zn and S) precursor can be added, prompting shell growth that effectively encapsulates the isocrystalline core and the dopants. Structurally and optically the shell/core particles behave like aged

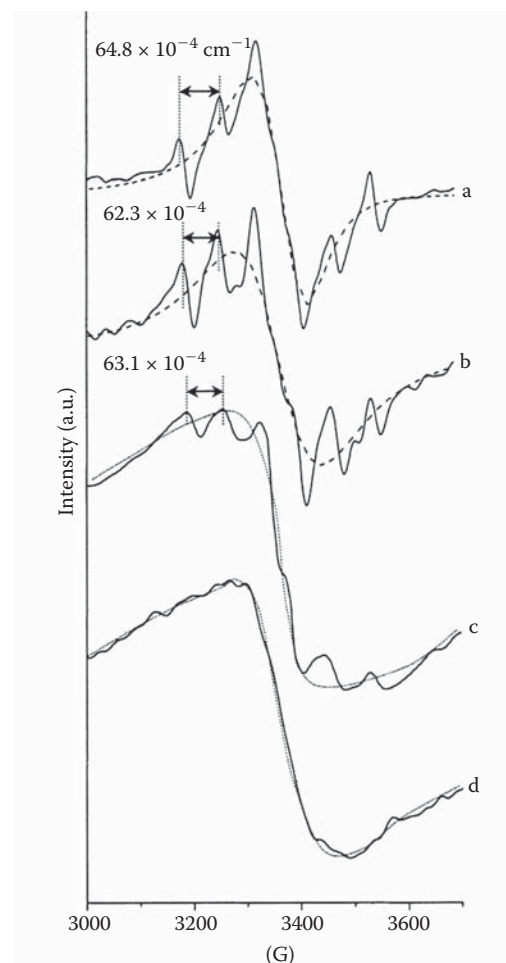


FIGURE 1.29 EPR spectra for $\text{Cd}_{1-x}\text{Mn}_x\text{S}$ nanorods. (a) $x = 0.02$. (b) $x = 0.04$. (c) $x = 0.08$. (d) $x = 0.12$. Hyperfine splitting due to Mn ($I = 5/2$) is evident in (a–c). The background Lorentzian-curve pattern is attributed to Mn–Mn interactions. (Reprinted with permission from Jun, Y., Y. Jung, and J. Cheon, *J. Am. Chem Soc.*, 124, 615, 2002.)

particles (better resolved hyperfine EPR signals and improved Mn^{2+} PL). Ligand-field electronic absorption spectroscopy was also used to distinguish between surface- and lattice-bound dopant ions, regardless of whether incorporation of ions into the host matrix occurred as a result of aging or isocrystalline shell growth (Figure 1.31).¹¹⁵

An additional factor that likely strongly influences NQD doping is ionic radii mismatch. The apparent relative ease with which a high-temperature solution-based synthesis method was used to prepare internally doped $\text{Zn}(\text{Mn})\text{Se}$ DMSs¹⁰⁷ may, in large part, be attributable to the size matching of the core metal and dopant

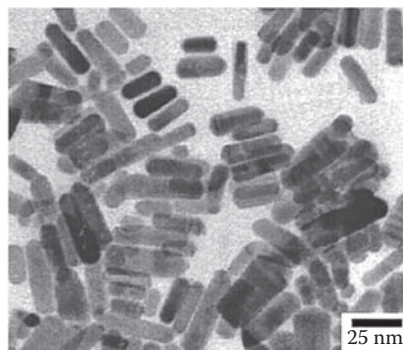


FIGURE 1.30 TEM of $\text{Cd}_{0.88}\text{Mn}_{0.12}\text{S}$ rods, 7 nm wide with an aspect ratio of ~4. (Reprinted with permission from Jun, Y., Y. Jung, and J. Cheon, *J. Am. Chem Soc.*, 124, 615, 2002.)

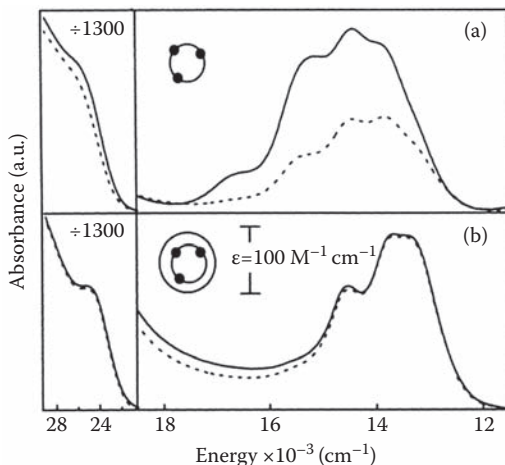


FIGURE 1.31 (a) Ligand-field absorption spectra (300 K) for 3.0 nm diameter $\text{Cd}_{1-x}\text{Co}_x\text{S}$ ($x = 0.023$) doped NQDs showing the CdS band-gap transitions (left panels) and the $\text{Co}^{2+} v_3$ ligand-field transitions (right panels). The NQDs were prepared by the standard coprecipitation method (see text) and subsequently suspended in pyridine. The spectra were taken 2 h (solid line) and 23 h (dashed line) after synthesis. The loss in Co^{2+} signal over time suggests that Co^{2+} is dissolving into the pyridine solvent. (b) Ligand-field absorption spectra (300 K) for 3.7 nm diameter $\text{Cd}_{1-x}\text{Co}_x\text{S}$ ($x = 0.009$) doped NQDs prepared by the isocrystalline (core)shell method, 2 h (solid line) and 28 h (dashed line) after synthesis. The reproducibility over time suggests that the (core)shell doped NQDs are stable to dissolution of Co^{2+} into the pyridine solvent. The absorption band shape of (a) is characteristic of Co^{2+} that resides on the CdS NQD surface, whereas that for (b) is characteristic of Co^{2+} that is incorporated into the crystal lattice structure of the host CdS. (Reprinted with permission from Radovanovic, P. V. and D. R. Gamelin, *J. Am. Chem Soc.*, 123, 12207, 2001.)

ionic radii: Zn²⁺(0.80 Å) and Mn²⁺(0.74 Å). In contrast, the relative difficulty of achieving even near-surface doping of Cd(Mn)Se by similar methods¹⁰⁵ may relate to the rather large size mismatch of the substituting cations: Cd²⁺(0.97 Å) and Mn²⁺(0.74 Å). Evidence from inverse-micelle preparations support this conclusion. Comparison of unaged Cd(Co)S and Zn(Co)S DMSs, where the ionic radius of Co²⁺ is 0.74 Å, revealed that the dopant is well distributed throughout the core lattice in the latter case, benefiting only minimally from an isocrystalline shell-growth step.

1.7 NANOCRYSTAL ASSEMBLY AND ENCAPSULATION

Owing to their chemical, size, shape, and properties tunability, NQDs have long been considered ideal building blocks for novel functional materials. Many conceived device applications require that NQDs be controllably assembled into organized structures, at a variety of length scales, and that these assemblies be macroscopically addressable. Even applications that make use of the optical properties of *individual* nanoparticles (e.g., fluorescent biolabeling) require controlled assembly of bio-nano conjugates. For these reasons, small- and large-scale assembly and encapsulation methods have been developed in which NQDs are manipulated as artificial atoms or molecules. Encapsulation has typically involved incorporating NQDs into organic polymers^{117–121} or inorganic glasses.^{122–124} Either may simply provide structural rigidity to an NQD ensemble, as well as protection from environmental degradation. Or, the matrix material may be electronically, optically, or magnetically “active,” where the encapsulant then provides for added functionality or device addressability. Assembly approaches are as diverse as the targeted applications and have emerged from each of the traditional disciplines: physics/physical chemistry (e.g., self-assembly approaches), chemistry (chemical patterning of surfaces, e.g., dip-pen nanolithography^{125,126} and electric-field directed assembly,¹²⁷) biology (e.g., bio-inspired mineralization¹²⁸ and DNA-directed assembly,^{126,129}) and materials science (e.g., lithography-defined templating.¹³⁰) The diversity of approaches suggests that the subject warrants a book of its own. Therefore, only a small subset of this field is reviewed here, namely, self-assembly at the nanoscale.

Particles uniform in size, shape, composition, and surface chemistry can self-assemble from solution into highly ordered 2-D and 3-D solids ([Figure 1.32](#)). The process is similar for particles ranging in size from cluster molecules to micron-sized colloidal particles.⁸ It entails controlled destabilization and precipitation from a slowly evaporating solvent ([Figure 1.33](#)). As the solution concentrates, interactions between particles become mildly attractive. Particle association is sufficiently slow, however, to prevent disordered aggregation. Instead, ordered assembly dominates by a reversible process of particle addition to the growing SL.¹⁰ Fully formed ordered solids are commonly called colloidal crystals ([Figure 1.34](#)), where the cluster, NQD, or colloid serves as the “artificial atom” building block. In the case of NQDs, the process is controlled by manipulating the polarity and the boiling point of the solvent.¹⁰ The solvent polarity is chosen to ensure that mild attractive forces develop between the nanoparticles as the solvent evaporates. The boiling point is chosen to ensure that the evaporation process is sufficiently slow.¹⁰ At the other extreme of very fast

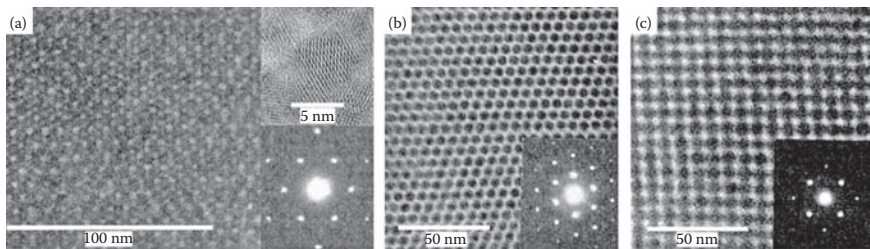


FIGURE 1.32 TEMs and ED patterns for CdSe NQD SLs of different orientations. (a) Main: $\langle 111 \rangle_{\text{SL}}$ -oriented array of 6.4 nm-diameter NQDs five layers thick. Upper right: HR-TEM of a single NQD with its $\langle 110 \rangle$ axis parallel to the electron beam and its $\langle 002 \rangle$ axis in the plane of the SL. Lower right: small-angle ED pattern. (b) Main: fcc array of 4.8 nm diameter NQDs ($\langle 101 \rangle_{\text{SL}}$ projection). Lower right: small-angle ED pattern. (c) Main: fcc array of 4.8 nm diameter NQDs ($\langle 100 \rangle_{\text{SL}}$ oriented). Lower right: small-angle ED pattern. (Reprinted with permission from Murray, C. B., C. R. Kagan, and M. G. Bawendi, *Science*, 270, 1335, 1995.)

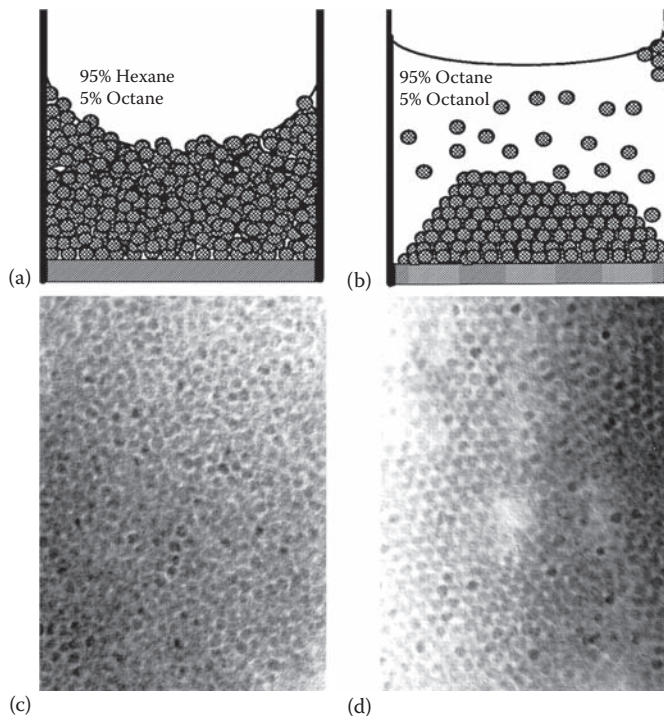


FIGURE 1.33 (a and b) Schematics illustrating the deposition conditions (solvent dependent) that yield 3-D, close-packed NQD solids (films nucleated heterogeneously at a surface or colloidal crystals nucleated homogeneously from solution) as (a) disordered glasses and (b) ordered SLs. (c and d) TEMs revealing the long-range disorder characteristic of the glassy solids (c) and the long-range order characteristic of the crystalline solids (d). (Reprinted with permission from Murray, C. B., C. R. Kagan, and M. G. Bawendi, *Annu. Rev. Mater. Sci.*, 30, 545, 2000.)

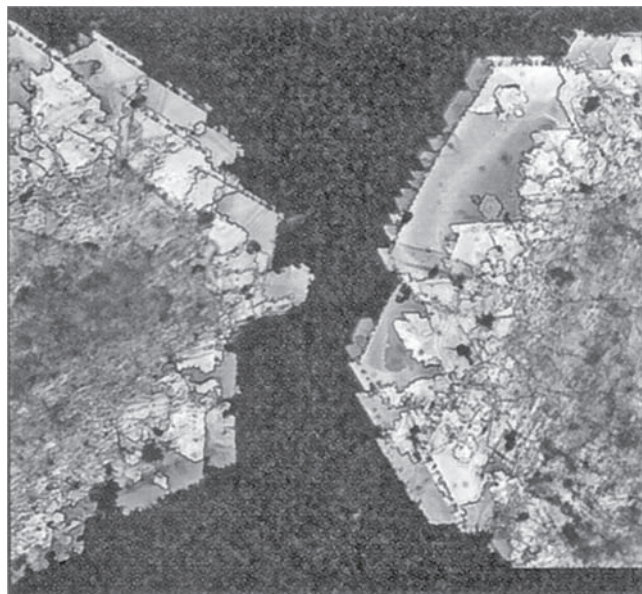


FIGURE 1.34 Dark-field optical micrograph of faceted CdSe colloidal crystals. The crystals were prepared by slow self-assembly of 2.0 nm diameter NQDs that nucleated homogeneously from solution. A mixed nonpolar/polar solvent system similar to that depicted in Figure 1.29b was used in combination with careful regulation of solution temperature and pressure to provide the necessary conditions for controlled destabilization of the NQD starting solution. The colloidal crystals are stacked and range in size from 5 to 50 μm . (Reprinted with permission from Murray, C. B., C. R. Kagan, and M. G. Bawendi, *Science*, 270, 1335, 1995.)

destabilization, by fast solvent evaporation or nonsolvent addition, a rapid increase in the “sticking coefficient” (particle attraction) and in the rate at which particles are added to the growing surface yields loosely associated fractal aggregates. Moderate destabilization rates, implemented by using moderate-boiling solvents, produce close-packed glassy solids having local order but lacking long-range order (Figure 1.33a).⁸ For assembly of well-ordered NQD SLs, the chosen solvent is typically a mixed solvent, involving both a lower-boiling alkane and a higher-boiling alcohol. The alkane evaporates more quickly than the alcohol, yielding relatively higher concentrations of the “destabilizing” alcohol (assuming the NQDs are surface terminated with long-chain alkyls) over time (Figure 1.33b).⁸ The process can be controlled by applying heat or vacuum to the system. Free-standing and surface-bound colloidal (fcc) crystals exhibiting long-range order over hundreds of microns have been prepared in this way. In addition, the individual NQDs can crystallographically orient as demonstrated by small-angle x-ray scattering and WAXS for a CdSe NQD thin film in which the wurtzite *c*-axis of the nanocrystals are aligned in the plane of the substrate.^{8,131}

Slow, controlled precipitation of highly ordered colloidal crystals has also been achieved by the method of “controlled oversaturation.”¹³² Here, gentle destabilization

is induced by slow diffusion of a nonsolvent into a NQD solution directly or through a “buffer” solution. The nonsolvent (e.g., methanol), buffer (e.g., propan-2-ol, if present), and the NQD solution (e.g., toluene solvent) are carefully layered in reaction tubes (**Figure 1.35a**). Colloidal-crystal nucleation occurs on the tube walls and in the bulk solution. Though both methods, not-buffered and buffered, yield well-ordered colloidal crystals from 100–200 microns in size; the latter process is relatively more controlled and produces faceted, hexagonal platelets (**Figure 1.35c**), rather than ragged, irregularly shaped colloidal crystals (**Figure 1.35b**). The CdSe NQD building blocks again yield (fcc) SLs.¹³²

Perhaps the most impressive demonstration of the power of controlled self-assembly to form ordered NQD arrays has been the recent utilization of the approach to prepare *binary and quasi-ternary* SLs.^{133–135} Combinations of semiconducting, metallic, and magnetic nanocrystals have now been induced to organize into “binary nanoparticle superlattices” (BNSLs) or,¹³⁴ in the case of multicomponent (iron)iron oxide hollow shell “nested” nanoparticles combined with gold nanoparticles, into quasi-“ternary nanoparticle superlattices” (TNSLs).¹³⁵ The forces controlling these BNSL and TNSL self-assembly processes are many and include van der Waals, electrostatic, steric repulsion, and directional dipolar interactions, which contribute to the interparticle potential, as well as effects of particle–substrate interactions and space-filling (entropic) contributions.¹³⁴ The ability to tune both the properties of the individual nanocrystal building blocks, as well as their assembly, is likely to have significant ramifications for the application of these nanomaterials. Namely, by combining nanocrystals in this way, new materials—the so-called “metamaterials”—are made possible, where metamaterials possess novel, “emergent” properties as a result of the collective interactions of the nanoscale building blocks.¹³³

In the self-assembly of large colloidal crystals from nano-sized crystals, the nanocrystals behave as artificial atoms. The self-assembly process is largely driven by the relative favorability of the interaction between the NQD surface *ligands* and the solvent.

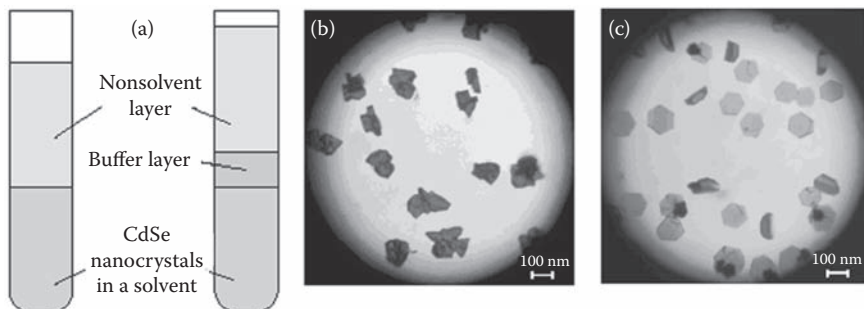


FIGURE 1.35 (a) Schematic illustrating the method of “controlled oversaturation” for the preparation of CdSe NQD colloidal crystals. (b) Optical micrograph of irregularly shaped colloidal crystals prepared without a buffer-solvent layer, that is, faster nucleation. (c) Optical micrograph of faceted hexagonal colloidal crystals prepared with a buffer-solvent layer, that is, slower nucleation. (Reprinted with permission from Talapin, D. V., E. V. Shevchenko, A. Kornowski, N. Gaponik, M. Haase, A. L. Rogach, and H. Weller, *Adv. Mater.*, 13, 1868, 2001.)

Without a favorable interaction, particle cores begin to attract via van der Waals forces. Nanoparticles can also assemble into large crystals by a self-assembly process called “oriented attachment.” In contrast with self-assembly by ligand-stabilized colloids, oriented attachment entails direct interaction between ligand-free (or almost ligand-free) nanocrystals.¹³⁶ The driving force for the assembly is the *lack* of surface-passivating ligands. The bare nanoparticles assemble to satisfy surface dangling bonds, and the assembly process is sufficiently reversible that *oriented* attachment dominates, leading to highly crystalline macrostructures. Oriented attachment is known in a variety of systems, including natural mineral systems where chains and extended sheets are formed,¹³⁷ epitaxial attachment of metal nanoparticles to metal substrates through a process of dislocation formation/movement and particle rotation in response to interfacial strain,¹³⁸ chain formation from nanoscale TiO₂ building blocks (Figure 1.36),¹³⁹ ZnO rod formation from ZnO nanodots,¹³⁶ and sheet formation from nanoscale rhombohedral InS and InSe building blocks.¹⁰⁴ This crystal-growth mechanism may even provide an advantage compared to traditional atom-by-atom growth, as nanoscale inorganic building blocks are typically characterized by nearly perfect or perfect crystal structures, devoid of internal defects. Constructing large crystals from these preformed perfect crystallites may permit growth of extended solids having unusually low defect densities.¹⁴⁰ Alternatively, impurities (natural and intentional dopants) can perhaps be more easily incorporated into large crystals by oriented attachment of nanocrystals decorated with surface impurities.^{137,140} Various types of dislocations, from edge to screw, can form as a result of interfacial distortions generated to accommodate coherency between surfaces that are not atomically flat (Figure 1.37). Thus, the forces driving particles to attach, that is, the drive to eliminate unsaturated surface bonds, can induce dislocation formation (Figure 1.38).¹⁴¹ Predictably, attachment occurs on high-surface-energy faces.¹⁴¹ For example, the rhombohedral InS (R-InS) and InSe

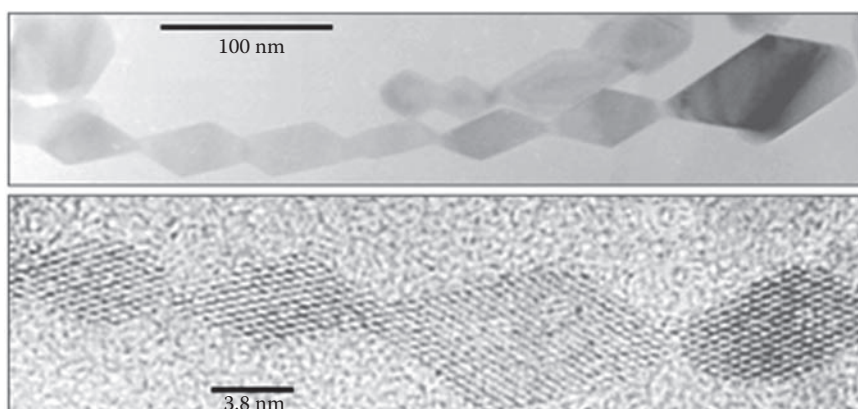


FIGURE 1.36 TEM of TiO₂ nanocrystal aggregates that have assembled by oriented attachment. The chains are oriented by a process of particle docking, aligning, and fusing. (Reprinted with permission from Penn, R. L. and J. F. Banfield, *Geochimica et Cosmochimica Acta*, 63, 1549, 1999.)

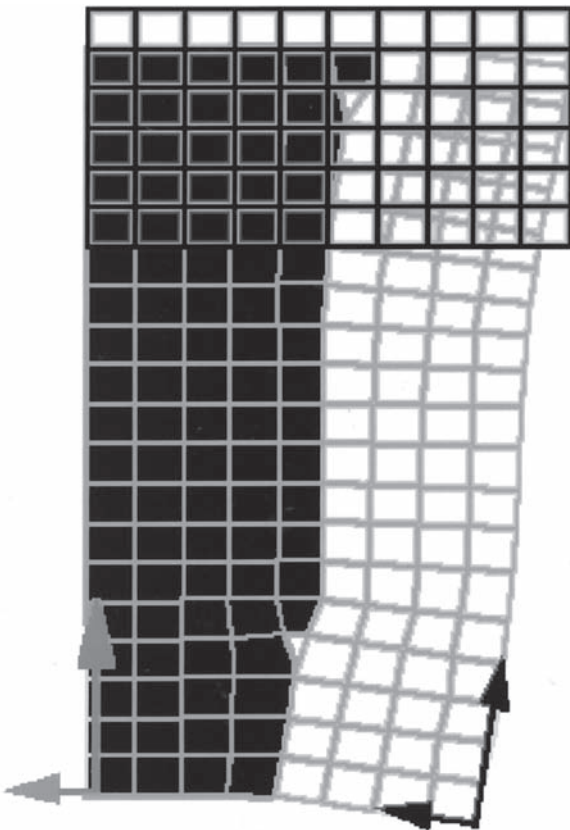


FIGURE 1.37 Schematic illustrating the process of dislocation generation in imperfect oriented attachment. Three particles are shown. First, the two lower particles join with a small rotation being incorporated as a result of surface steps on the particle to the left. The third particle joins in an oriented fashion to the left-side crystal, but with a rotational misorientation relative to the right-side crystal. The diagram demonstrates the formation of two types of dislocations: edge (dislocation line normal to the page) and screw (dislocation line horizontal). (Reprinted with permission from Penn, R. L. and J. F. Banfield, *Science*, 281, 969, 1998.)

(R-InSe) crystal structures feature planar, covalently bonded sheets that are four atomic layers thick and are separated by van der Waals gaps. Solution-phase growth at low temperature ($\sim 200^\circ\text{C}$) generates nanocrystal platelets (5–20 nm) that self-assemble, or “self-attach,” to form large micron-scale sheets. The underlying pseudographitic layered structure supports growth of nanocrystals in the form of 2-D platelets. The van der Waals surfaces of the nanocrystal *ab* plane (the large-area plane in the platelets) are low-energy, coordinatively saturated faces, whereas the edges of the nanocrystallites are characterized by higher-energy unsaturated sites. Therefore, it is at the edges that the nanoplatelets likely attach, generating the larger sheets. Electron diffraction (ED) patterns collected perpendicular to the large-area sheet surfaces and over large areas (collection radii ≈ 150 nm) demonstrate not only that the crystallographic *c* axes

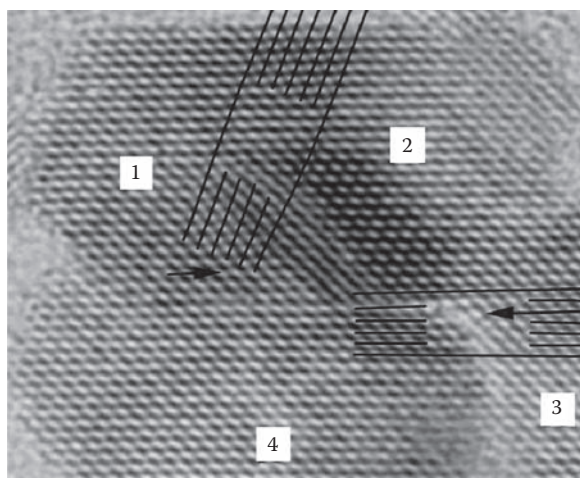


FIGURE 1.38 HR-TEM (along [100] TiO_2 anatase) of a crystal segment formed by oriented attachment of at least four particles (numbered 1–4). Arrowheads and lines (0.48 nm apart) show edge dislocations. (Reprinted with permission from Penn, R. L. and J. F. Banfield, *Science*, 281, 969, 1998.)

are indeed perpendicular to the sheet surfaces but also that the sheets diffract coherently, as single crystals would (Figure 1.39). Assembly and attachment of platelets into sheets, therefore, proceeds in a crystallographically coherent fashion.¹⁰⁴

Nanocrystal self-assembly can also proceed by way of *electrostatic or covalent interactions*. In a recent example, oppositely charged CdS nanocrystals were mixed in different ratios and under controlled ionic strength. The positively charged

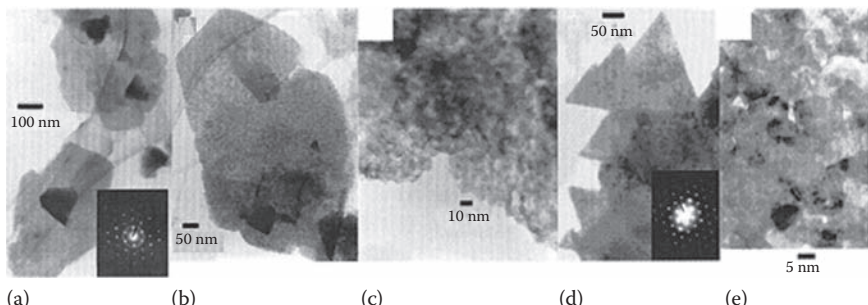


FIGURE 1.39 TEMs of InSe and InS colloidal-crystal platelets formed by oriented assembly of nanosized building blocks. (a) InSe platelets approximating hexagonal shapes; inset, electron-diffraction pattern collected along the [0001] zone axis of a platelet. (b) InSe platelet revealing texture. (c) InSe platelet edge revealing constituent hexagonal nanocrystallites. (d) InS platelets with triangular features; inset, electron-diffraction pattern collected along the [0001] zone axis of a platelet. (e) InS platelet center revealing internal structure. (Reprinted with permission from Hollingsworth, J. A., D. M. Poorjay, A. Clearfield, and W. E. Buhro, *J. Am. Chem. Soc.*, 122, 3562, 2000.)

CdS nanocrystals were prepared by surface modification with 2-(dimethylamino) ethanethiol, while the negatively charged nanocrystals were surface passivated with 3-mercaptopropionic acid. At high ionic strength, the particles repelled one another, regardless of relative particle concentrations, whereas at low ionic strength oppositely charged particles developed an attractive potential. When present in equal proportions, the negatively and positively charged particles aggregated and precipitated from solution. Despite imperfect size dispersions and some differences in size between the oppositely charged particles, ordering was observed by low-angle XRD. Consistent with self-assembly from nonpolar solvent systems, the degree of ordering in these aqueous-based systems was enhanced by slowing the precipitation rate. Also, when the positively and negatively charged particles were present in unequal amounts, for example, ratios of 1:10, soluble molecule-like clusters were formed. These comprised a central particle of one charge surrounded by several particles of opposite charge. CdS–CdS clusters were demonstrated as were CdS-coated Au particles.¹⁴²

In a recent example of covalently driven assembly, disordered but densely packed CdSe nanocrystal monolayers were deposited onto *p*- and *n*-doped GaAs substrates. The GaAs substrates were either bare or pretreated with dithiol self-assembled monolayers (SAMs). In the absence of the 1,6-hexanedithiol layer, the NQDs were only physically absorbed into the substrate and did not withstand a thorough toluene wash. In contrast, NQDs self-assembled onto the dithiol SAMs were very robust due to covalent linkages between the NQDs and the exposed thiols.¹⁴³ Soluble, covalently linked NQD clusters have also been prepared. Dimers and larger-order NQD “molecules” were prepared from dilute solutions in which bifunctional linkers provided covalent attachment between two or several CdSe NQDs.¹⁴⁴ Improving yields and enhancing control over “molecule” size (dimer versus trimer, etc.) remain as future challenges.

Both electrostatic and covalent linkage strategies have been applied to biological labeling applications where fluorescent NQDs provide specific tags for cellular constituents.¹⁴⁵ The NQDs are negatively charged using, for example, either dihydroliptic acid (DHLA)¹⁴⁶ or octylamine-modified polyacrylic acid¹⁴⁷ as a surface capping agent (**Figure 1.40**). In the former case, positively charged proteins are coupled *electrostatically* directly to the negatively charged NQD or indirectly through a positively charged leucine zipper peptide bridge.¹⁴⁶ In the latter case, coupling to antibodies, streptavidin, or other proteins is *covalent* to the polyacrylate cap via traditional carbodiimide chemistry.¹⁴⁷ Both the DHLA and the polyacrylate methods provide relatively simple NQD surface-modification procedures for achieving biological compatibility, that is, retention of high QYs in PL, pathways for specific binding to biological targets, and biological inertness.¹⁴⁵

The preceding methods for NQD self-assembly represent only a fraction of this growing field. As such, they are not meant to be inclusive; rather, they are intended to provide theoretical background for understanding the chemical and physical issues involved in the assembly process and to highlight possible future directions for research. Further, we have intentionally avoided discussion of templated, directed, and active assembly of nanoscale building blocks, as this area is perhaps even more diverse and remains a subject of intense and active investigation.

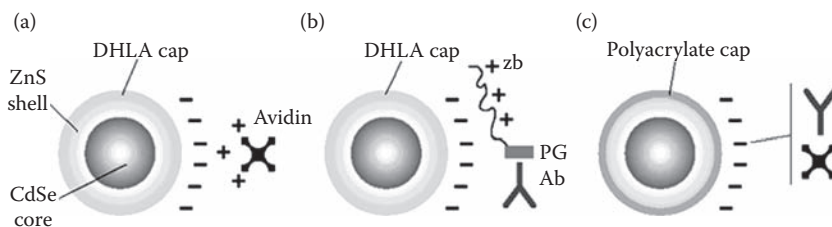


FIGURE 1.40 Three strategies for bioconjugation to NQDs. Highly luminescent (CdSe/ZnS) core-shell NQDs comprise the fluorescent probe. The NQD surfaces are negatively charged using the carboxylate groups of either dihydrolipoic acid (DHLA) (a and b) or an amphiphilic polymer (40% octylamine modified polyacrylic acid) (c). In (a and b), proteins are conjugated electrostatically to the DHLA-NQDs either (a) directly or (b) indirectly via a bridge comprising a positively charged leucine zipper peptide, zb, fused to a recombinant protein, PG, that binds to a primary antibody, Ab, with target specificity. In (c), covalent binding by way of traditional carbodiimide chemistry is used to couple antibodies, streptavidin, or other proteins to the polyacrylate cap. Adapted in part and Reprinted with permission from Jaiswal, J. K., H. Mattoussi, J. M. Mauro, and S. M. Simon, *Nat. Biotech.*, 21, 47, 2003.)

ACKNOWLEDGMENT

We would like to acknowledge Jennifer's husband, Howard Coe, for editing the text, transcribing and organizing references, and making graphical improvements to the figures. Jennifer would also like to thank Howard for his patience, support, and sense of humor throughout this project.

REFERENCES

1. Petroff, P. M. and Medeiros-Ribeiro, G. (1996) *MRS Bull.* 21, 54.
2. Bimberg, D., Grundmann, M., and Ledentsov, N. N. (1998) *MRS Bull.* 23, 31.
3. Yoffe, A. D. (2001) *Adv. Phys.* 50, 1.
4. Hu, J., Odom, T. W., and Lieber, C. M. (1999) *Acc. Chem. Res.* 32, 435.
5. Lauhon, L. J., Gudiksen, M. S., Wang, D., and Lieber, C. M. (2002) *Nature* 420, 57.
6. Borelli, N. F. and Smith, D. W. (1994) *J. Non-Crystalline Solids* 180, 25.
7. Lipovskii, A., Kolobkova, E., Petrikov, V., Kang, I., Olkhovets, A., Krauss, T., Thomas, M., Silcox, J., Wise, F., Shen, Q., and Kycia, S. (1997) *App. Phys. Lett.* 71, 3406.
8. Murray, C. B., Kagan, C. R., and Bawendi, M. G. (2000) *Annu. Rev. Mater. Sci.* 30, 545.
9. La Mer, V. K. and Dinegar, R. H. (1950) *J. Am. Chem. Soc.* 72, 4847.
10. Murray, C. B., Sun, S., Gaschler, W., Doyle, H., Betley, T. A., and Kagan, C. R. (2001) *IBM J. Res. Dev.* 45, 47.
11. Liu, H., Owen, J. S., and Alivisatos, A. P. (2007) *J. Am. Chem. Soc.* 129, 305–312.
12. Steckel, J. S., Yen, B. K. H., Oertel, D. C., and Bawendi, M. G. (2006) *J. Am. Chem. Soc.* 128, 13032–13033.
13. van Embden, J. and Mulvaney, P. (2005) *Langmuir* 21, 10226.
14. Thessing, J., Qian, J., Chen, H., Pradhan, N., and Peng, X. (2007) *J. Am. Chem. Soc.* 129, 2736.
15. Xie, R. and Peng, X. (2008) *Angew. Chem. Int. Ed.* 47, 7677.

16. Nozik, A. J. and Micic, O. I. (1998) *MRS Bull.* 23, 24.
17. Peng, Z. A. and Peng, X. (2001) *J. Am. Chem Soc.* 123, 1389.
18. Higginson, K. A., Kuno, M., Bonevich, J., Qadri, S. B., Yousuf, M., and Mattossi, H. (2002) *J. Phys. Chem.* 106, 9982.
19. Peng, X., Wickham, J., and Alivisatos, A.P. (1998) *J. Am. Chem Soc.* 120, 5343.
20. Murray, C. B., Norris, D. J., and Bawendi, M. G. (1993) *J. Am. Chem Soc.* 115, 8706.
21. Qu, L., Peng, Z. A., and Peng, X. (2001) *Nano Lett.* 1, 333.
22. Peng, X., Manna, L., Yang, W., Wickham, J., Scher, E., Kadavanich, A., and Alivisatos, A.P. (2000) *Nature* 404, 59.
23. Wehrenberg, B. L., Wang, C. J., and Guyot-Sionnest, P. (2002) *J. Phys. Chem. B*, 106, 10634.
24. Qu, L. and Peng, X. G. (2002) *J. Am. Chem Soc.* 124, 2049.
25. Hines, M. and Guyot-Sionnest, P. (1998) *J. Phys. Chem. B* 102, 3655.
26. Peng, X., Schlamp, M. C., Kadavanich, A. V., and Alivisatos, A.P. (1997) *J. Am. Chem. Soc.* 119, 7019.
27. Pietryga, J. M., Schaller, R. D., Werder, D. Stewart, M. H., Klimov, V. I., and Hollingsworth, J. A. (2004) *J. Am. Chem. Soc.* 126, 11752.
28. Kershaw, S. V., Harrison, M., Rogach, A. L., and Kornowski, A. (2000) *J. Selected Top. in Quantum Elect.* 6, 534.
29. Gao, S., Lu, J., Chen., N., Zhao, Y., and Xie, Y. (2002) *Chem. Commun.* 3064.
30. Gaponik, N., Talapin, D. V., Rogach, A. L., Hoppe, K., Shevchenko, E. V., Kornowski, A., Eychmüller, A., and Weller, H. (2002) *J. Phys. Chem. B* 106, 7177.
31. Vossmeyer, T., Katsikis, L., Giersig, M., Popovic, I. G., Diesner, K., Chemseddine, A., Eychmüller, A., and Weller, H. (1994) *J. Phys. Chem.* 98, 7665.
32. Rogach, A., Kershaw, S., Burt, M., Harrison, M., Kornowski, A., Eychmüller, A., and Weller, H. (1999) *Adv. Mater.* 11, 552.
33. Rockenberger, J., Troger, L., Rogach, A. L., Tischer, M., Grundmann, M., Eychmüller, A., and Weller, H. (1998) *Ber. Bunsenges Phys. Chem.* 102, 1.
34. Steigerwald, M. L., Alivisatos, A. P., Gibson, J. M., Harris, T. D., Kortan, R., Muller, A. J., Thayer, A. M., Duncan, T. M., Douglas, D. C., and Brus, L. E. (1988) *J. Am. Chem. Soc.* 110, 3046.
35. O'Brien, S., Brus, L., and Murray, C. B. (2001) *J. Am. Chem. Soc.* 123, 12085.
36. Hines, M. A. and Guyot-Sionnest, P. (1996) *J. Phys. Chem.* 100, 468.
37. Dabbousi, B. O., Rodriguez-Viejo, J., Mikulec, F. V., Heine, J. R., Mattossi, H., Ober, R., Jensen, K. F., and Bawendi, M. G. (1997) *J. Phys. Chem. B* 101, 9463.
38. Micic, O. I., Smith, B. B., and Nozik, A. J. (2000) *J. Phys. Chem. B* 104, 12149.
39. Cao, Y. W. and Banin, U. (1999) *Agnew. Chem. Int. Ed.* 38, 3692.
40. Cao, Y. W. and Banin, U. (2000) *J. Am. Chem. Soc.* 122, 9692.
41. Li, J. J., Wang, Y. A., Guo, W., Keay, J. C., Mishima, T. D., Johnson, M. B., and Peng, X. (2003) *J. Am. Chem. Soc.* 125, 12567.
42. Xie, R., Kolb, U., Li, J., Basch, T., and Mews, A. (2005) *J. Am. Chem. Soc.* 127, 7480.
43. Chen, Y., Vela, J., Htoon, H., Casson, J. L., Werder, D. J., Bussian, D. A., Klimov, V. I., and Hollingsworth, J. A. (2008) *J. Am. Chem. Soc.* 130, 5026.
44. Pietryga, J. M., Werder, D. J., Williams, D. J., Casson, J. L., Schaller, R. D., Klimov, V. I., and Hollingsworth, J. A. (2008) *J. Am. Chem. Soc.* 130, 4879.
45. Son, D. H., Hughes, S. M., Yin, Y., and Alivisatos, A. P. (2004) *Science* 306, 1009.
46. Hohng, S. and Ha, T. (2004) *J. Am. Chem. Soc.* 126, 1324.
47. Hammer, N. I., Early, K. T., Sill, K., Odoi, M. Y., Emrick, T., and Barnes, M. D. (2006) *J. Phys. Chem. B* 110, 14167.
48. He, H., Qian, H., Dong, C., Wang, K., and Ren, J. (2006) *Angew. Chem. Int. Ed.* 45, 7588.

49. Jeong, S., Achermann, M., Nanda, J., Ivanov, S., Klimov, V. I., and Hollingsworth, J. A. (2005) *J. Am. Chem. Soc.* 127, 10126.
50. Heyes, C. D., Kobitski, A. Yu., Breus, V. V., and Nienhaus, G. U. (2007) *Phys. Rev. B* 75, 125431.
51. Pistol, M-E., Castrillo, P., Hessman, D., Prieto, J. A., and Samuelson, L. (1999) *Phys. Rev. B* 59, 10725.
52. Mahler, B., Spinicelli, P., Buil, S., Quelin, X., Hermier, J.-P., and Dubertret, B. (2008) *Nat. Mater.* 7, 659.
53. Vela, J., Chen, Y., Casson, A., Htoon, H., and Hollingsworth, J. A. unpublished data.
54. Eychmüller, A., Mews, A., and Weller, H. (1993) *Chem. Phys. Lett.* 208, 59.
55. Mews, A., Eychmüller, A., Giersig, M., Schoos, D., and Weller, H. (1994) *J. Phys. Chem.* 98, 934.
56. Mews, A., Kadavanich, A. V., Banin, U., and Alivisatos, A.P. (1996) *Phys. Rev. B* 53, R13242.
57. Little, R. B., El-Sayed, M. A., Bryant, G. W., and Burke, S. (2001) *J. Chem. Phys.* 114, 1813.
58. Kim, S., Fisher, B., Eisler, H.-J., and Bawendi, M. (2003) *J. Am. Chem. Soc.* 125, 11466.
59. Schöps, O., Le Thomas, N., Woggon, U., and Artemyev, M. V. (2006) *J. Phys. Chem. B* 110, 2074.
60. Yu, K., Zaman, B., Romanova, S., Wang, D., and Ripmeester, J. (2005) *Small* 1, 332.
61. Xie, R., Zhong, X. and Basché, T. (2005) *Adv. Mater.* 17, 2741.
62. Ivanov, S. A., Nanda, J., Piryatinski, A., Achermann, M., Balet, L. P., Bezel, I. B., Anikeeva, P. O., Tretiak, S., and Klimov, V. I. (2004) *J. Phys. Chem. B* 108, 10625.
63. Ivanov, S. A., Piryatinski, A., Nanda, J., Tretiak, S., Zavadil, K. R., Wallace, W. O., Werder, D., and Klimov, V. I. (2007) *J. Am. Chem. Soc.* 129, 11708.
64. Manna, L., Scher, E. C., and Alivisatos, A.P. (2000) *J. Am. Chem. Soc.* 122, 12700.
65. Kazes, M., Lewis, D. Y., Ebenstein, Y., Mokari, T., and Banin, U. (2002) *Adv. Mater.* 14, 317.
66. Manna, L., Scher, E. C., Li, L. S., and Alivisatos, A.P. (2002) *J. Am. Chem Soc.* 124, 7136.
67. Jun, Y., Lee, S. M., Kang, N. M., and Cheon, J. (2001) *J. Am. Chem Soc.* 123, 5150.
68. Jun, Y., Jung, Y., and Cheon, J. (2002) *J. Am. Chem Soc.* 124, 615.
69. Lee, S. M., Jun, Y., Cho, S. N., and Cheon, J. (2002) *J. Am. Chem Soc.* 124, 11244.
70. Manna, L., Milliron, D. J., Meisel, A., Scher, E. C., and Alivisatos, A. P. (2003) *Nat. Mater.* 2, 382.
71. Mokari, T., Rothenberg, E., Popov, I., Costi, R., and Banin, U. (2004) *Science* 304, 1787.
72. Shieh, F., Saunders, A. E., and Korgel, B. A. (2005) *J. Phys. Chem. B* 109, 8538.
73. Halpert, J. E., Porter, V. J., Zimmer, J. P., and Bawendi, M. G. (2006) *J. Am. Chem. Soc.* 128, 12590.
74. Talapin, D. V., Nelson, J. H., Shevchenko, E. V., Aloni, S., Sadtler, B., and Alivisatos, A. P. (2007) *Nano Lett.* 7, 2951.
75. Kumar, S., Jones, M., Lo, S. S., and Scholes, G. D. (2007) *Small* 3, 1633.
76. Koo, B. and Korgel, B. A. (2008) *Nano Lett.* 8, 2490.
77. Milliron, D., Hughes, S. M., Cui, Y., Manna, L., Li, J., Wang, L.-W., and Alivisatos, A. P. (2004) *Nature* 430, 190.
78. Xie, R., Kolb, U., and Basché, T. (2006) *Small* 2, 1454.
79. Yong, K.-T., Sahoo, Y., Swihart, M. T., and Prasad, P. N. (2006) *Adv. Mater.* 18, 1978.
80. Trentler, T. J., Hickman, K. M., Goel, S. C., Viano, A. M., Gibbons, P. C., and Buhro, W. E. (1995) *Science* 270, 1791.

81. Yu, H. and Buhro, W. E. (2003) *Adv. Mater.* 15, 416.
82. Yu, H., Li, J., Loomis, R. A., Wang, L.-W., and Buhro, W. E. (2003) *Nat. Mater.* 2, 517.
83. Yu, H., Gibbons, P. C., Kelton, K. F., and Buhro, W. E. (2001) *J. Am. Chem Soc.* 123, 9198.
84. Grebinski, J. W., Hull, K. L., Zhang, J., Kodel, T. H., and Kuno, M. (2004) *Chem. Mater.* 16, 5260.
85. Holmes, J. D., Johnston, K. P., Doty, R. C., and Korgel, B. A. (2000) *Science* 287, 1471.
86. Wang, F., Dong, A. Sun, J., Tang, R., Yu, H., and Buhro, W. E. (2006) *Inorg. Chem.* 45, 7511.
87. Kuno, M. (2008) *Phys. Chem. Chem. Phys.* 10, 620.
88. Dong, A., Wang, F. D., Daulton, T. L., and Buhro, W. E. (2007) *Nano Lett.* 7, 1308.
89. Ouyang, L., Maher, K. N., Yu, C. L., McCarty, J., and Park, H. (2007) *J. Am. Chem. Soc.* 129, 133.
90. Dong, A., Tang, R., and Buhro, W. E. (2007) *J. Am. Chem. Soc.* 129, 12254.
91. Chen, C. C., Herhold, A. B., Johnson, C. S., and Alivisatos, A.P. (1997) *Science* 276, 398.
92. Wickham, J. N., Herhold, A. B., and Alivisatos, A.P. (2000) *Phys. Rev. Lett.* 84, 923.
93. Herhold, A. B., Chen, C. C., Johnson, C. S., Tolbert, S. H., and Alivisatos, A.P. (1999) *Phase Trans.* 68, 1.
94. Jacobs, K., Zaziski, D., Scher, E. C., Herhold, A. B., and Alivisatos, A.P. (2001) *Science* 293, 1803.
95. Stein, A., Keller, S. W., and Mallouk, T. E. (1993) *Science* 259, 1558.
96. Buhro, W. E., Hickman, K. M., and Trentler, T. J. (1996) *Adv. Mater.* 8, 685.
97. Brus, L. (1997) *Science* 276, 373.
98. Parkinson, B. (1995) *Science* 270, 1157.
99. Switzer, J. A., Shumsky, M. G., and Bohannan, E. W. (1999) *Science* 284, 293.
100. Gillan, E. G. and Barron, A. R. (1997) *Chem. Mater.* 9, 3037.
101. Sellinschegg, H., Stuckmeyer, S. L., Hornbostel, M. D., and Johnson, D. C. (1998) *Chem. Mater.* 10, 1096.
102. Noh, M. and Johnson, D. C. (1996) *J. Am. Chem. Soc.* 118, 9117.
103. Noh, M., Thiel, J., and Johnson, D. C. (1995) *Science* 270, 1181.
104. Hollingsworth, J. A., Poorjay, D. M., Clearfield, A., and Buhro, W. E. (2000) *J. Am. Chem. Soc.* 122, 3562.
105. Mikulec, F. V., Kuno, M., Bennati, M., Hall, D. A., Griffin, R. G., and Bawendi, M. G. (2000) *J. Am. Chem. Soc.* 122, 2532.
106. Hoffman, D. M., Meyer, B. K., Ekimov, A. I., Merkulov, I. A., Efros, A. L., Rosen, M., Couino, G., Gacoin, T., and Boilot, J. P. (2000) *Sol. St. Comm.* 114, 547.
107. Norris, D. J., Yao, N., Charnock, F. T., and Kennedy, T. A. (2001) *Nano Lett.* 1, 3.
108. Bhargava, R. N., Gallagher, D., Hong, X., and Nurmiko, A. (1994) *Phys. Rev. Lett.* 72, 416.
109. Levy, L., Hochepied, J. F., and Pilani, M. P. (1996) *J. Phys. Chem.* 100, 18322.
110. Levy, L., Feltin, N., Ingert, D., and Pilani, M. P. (1999) *Langmuir* 15, 3386.
111. Couino, G., Esnouf, S., Gacoin, T., and Boilot, J. P. (1996) *J. Phys. Chem.* 100, 20021.
112. Ladizhansky, V., Hodes, G., and Vega, S. (1998) *J. Phys. Chem. B* 102, 8505.
113. Kim, K. W., Cowen, J. A., Dhingfa, S., and Kanatzidis, M. G. (1992) *Mater. Res. Soc. Symp.* 272, 27.
114. Bhargava, R. N. (1996) *J. Lumin.* 70, 85.
115. Radovanovic, P. V., and Gamelin, D. R. (2001) *J. Am. Chem Soc.* 123, 12207.
116. Levy, L., Ingert, D., Feltin, N., and Pilani, M. P. (1998) *Adv. Mater.* 10, 53.
117. Fogg, D. E., Radzilowski, L. H., Dabbousi, B. O., Schrock, R. R., Thomas, E. L., and Bawendi, M. G. (1997) *Macromolecules* 30, 8433.

118. Greenham, N. C., Peng, X., and Alivisatos, A.P. (1997) *Synthetic Metals* 84, 545.
119. Mattoussi, H., Radzilowski, L. H., Dabbousi, B. O., Fogg, D. E., Schrock, R. R., Thomas, E. L., Rubner, M. F., and Bawendi, M. G. (1999) *J. App. Phys.* 86, 4390.
120. Huynh, W. U., Peng, X., and Alivisatos, A.P. (1999) *Adv. Mater.* 11, 923.
121. Huynh, W. U., Dittmer, J. J., and Alivisatos, A.P. (2002) *Science* 295, 2425.
122. Sundar, V. C., Eisler, H. J., and Bawendi, M. G. (2002) *Adv. Mater.* 14, 739.
123. Eisler, H. J., Sundar, V. C., Bawendi, M. G., Walsh, M., Smith, H. I., and Klimov, V. I. (2002) *Appl. Phys. Lett.* 80, 4614.
124. Petruska, M. A., Malko, A. V., and Klimov, V. I. (2003) *Adv. Mater.*
125. Piner, R. D., Zhu, J., Xu, F., Hong, S., and Mirkin, C. A. (1999) *Science* 283, 661.
126. Mirkin, C. A. (2000) *Inorg. Chem.* 39, 2258.
127. Gao, M., Sun, J., Dulkeith, E., Gaponik, N., Lemmer, U. and Feldmann, J. (2002) *Langmuir* 18, 4098.
128. Sone, E. D., Zubarev, E. R., and Stupp, S. I. (2002) *Angew. Chem. Int. Ed.* 41, 1705.
129. Mitchell, G. P., Mirkin, C. A., and Letsinger, R. L. (1999) *J. Am. Chem Soc.* 121, 8122.
130. Hua, F., Shi, J., Lvov, Y., and Cui, T. (2002) *Nano Lett.* 2, 1219.
131. Murray, C. B., Kagan, C. R., and Bawendi, M. G. (1995) *Science* 270, 1335.
132. Talapin, D. V., Shevchenko, E. V., Kornowski, A., Gaponik, N., Haase, M., Rogach, A. L., and Weller, H. (2001) *Adv. Mater.* 13, 1868.
133. Redl, F. X., Cho, K.-S., Murray, C. B., and O'Brien, S. (2003) *Nature* 423, 968.
134. Shevchenko, E. V., Talapin, D. V., Kotov, N. A., O'Brien, S., and Murray, C. B. (2006) *Nature* 439, 55.
135. Shevchenko, E. V., Kortright, J. B., Talapin, D. V., Aloni, S., and Alivisatos, A. P. (2007) *Adv. Mater.* 19, 4183.
136. Pacholski, C., Kornowski, A., and Weller, H. (2002) *Angew. Chem. Int. Ed.* 41, 1188.
137. Banfield, J. F., Welch, S. A., Zang, H., Ebert, T. T., and Penn, R. L. (2000) *Science* 289, 751.
138. Zhu, H. L. and Averback, R. S. (1996) *Philos. Mag.* 73, 27.
139. Penn, R. L. and Banfield, J. F. (1999) *Geochimica et Cosmochimica Acta*, 63, 1549.
140. Alivisatos, A.P. (2000) *Science* 289, 736.
141. Penn, R. L. and Banfield, J. F. (1998) *Science* 281, 969.
142. Kolny, J., Kornowski, A., and Weller, H. (2002) *Nano Lett.* 2, 361.
143. Marx, E., Ginger, D. S., Walzer, K., Stokbro, K., and Greenham, N. C. (2002) *Nano Lett.* 2, 911.
144. Peng, X., Wilson, T. E., Alivisatos, A. P., and Schultz, P. G. (1997) *Angew. Chem. Int. Ed. Engl.* 36, 145.
145. Jovic, T. M. (2003) *Nat. Biotech.* 21, 32.
146. Jaiswal, J. K., Mattoussi, H., Mauro, J. M., and Simon, S. M. (2003) *Nat. Biotech.* 21, 47.
147. Wu, X., Liu, H., Liu, J., Haley, K. N. Treadway, J. A., Larson, P., Ge, N., Peale, F., and Bruchez, M. P. (2003) *Nat. Biotech.* 21, 41.